

Electronic Thesis and Dissertation Repository

---

11-7-2023 3:00 PM

# Temperature Mapping using Mid-Field Magnetic Resonance Imaging

Diego F. Martinez, *Western University*

Supervisor: Chronik, Blaine A., *The University of Western Ontario*

A thesis submitted in partial fulfillment of the requirements for the Doctor of Philosophy degree in Physics

© Diego F. Martinez 2023

Follow this and additional works at: <https://ir.lib.uwo.ca/etd>

---

## Recommended Citation

Martinez, Diego F., "Temperature Mapping using Mid-Field Magnetic Resonance Imaging" (2023). *Electronic Thesis and Dissertation Repository*. 9891.  
<https://ir.lib.uwo.ca/etd/9891>

This Dissertation/Thesis is brought to you for free and open access by Scholarship@Western. It has been accepted for inclusion in Electronic Thesis and Dissertation Repository by an authorized administrator of Scholarship@Western. For more information, please contact [wlsadmin@uwo.ca](mailto:wlsadmin@uwo.ca).

## Abstract

Magnetic Resonance Imaging (MRI) is a non-invasive imaging modality with excellent soft tissue contrast and sensitivity to tissue temperature. MRI use is growing in Canada with expectation that this is expected to continue in the medium term, with more wide adoption of MRI and in particular a renewed focus on MR systems which deviate from the most commonly used 1.5T field strength system. By implementing systems which do not use as strong magnets and instead operate  $<1T$ , many of the costs and requirements which burden the installation of MR systems can be alleviated.

Generally, as the field strength of an MR system decreases, the signal received when imaging also decreases, which makes it difficult to implement some applications which are standard at higher field. One such application is temperature mapping on a these  $<1T$  systems, which can be used to monitor thermal therapies interventionaly.

This thesis addresses the potentials for implementing temperature mapping at 0.5T, both in the creation of a tissue mimicking phantom which can be used to compare temperature mapping methods and implementing temperature maps both in vivo and in the custom phantom. As well, motivated by the sensitivity that thermal mapping has to external disturbances, the challenges that these accessible MR systems face when being in non-specialized environments is addressed, as this can potentially limit the efficacy of temperature mapping.

This work ultimately demonstrates the acceptable capabilities of a 0.5T system to map temperatures with an adequate temporal resolution, along with presenting practical solutions to operating a system in non-traditional locations.

## Keywords

Magnetic Resonance Imaging, Temperature mapping, MR Thermometry, Magnetic Field Stability, Echo Planar Imaging, Thermal Ablation, Spin Echo Imaging.

## Summary for Lay Audience

Magnetic Resonance Imaging, or MRI, is a medical imaging technique that helps doctors non-invasively probe the body. It's excellent at showing details of the tissues and organs inside the body and is sensitive to a variety of changes in the body, including changes to the temperature of tissues. Because of this, clinicians have been using standard MRIs to create maps of temperature, which can be used when treating a patient using tumor ablation or other thermal therapies. The use of these maps helps to track the amount of thermal dose being applied to a patient and can ensure that we are not applying too much or too little treatment. In Canada, the use of MRI is growing, and this trend is expected to continue.

Now, there's a new focus on making MRI machines that are different from the ones we usually see. These new MR systems use weaker magnets, which can make them less expensive and easier to install in places that aren't hospitals or other specialized imaging facilities. However, the tradeoff when using these magnets in places where they are less isolated from their environment is the images we get from MRI are not as clear, although using state of the art components can close much of the quality gap between these lower field systems and the standard counterparts.

This thesis is about finding ways to implement temperature mapping techniques on these lower field MRI systems, particularly at a field strength of 0.5T. We're creating models which accurately mimick properties of human tissue, we test how well temperatures can be measured, and figure out what challenges are faced when placing these MR systems in non-traditional settings like in remote areas or smaller clinics. This research is helping to make MRI more accessible and useful for everyone, while showing the capabilities of imaging on a lower field system can approach what is currently done at higher field strengths.

## Co-Authorship Statement

The following thesis comprises:

The work described in **Chapter 2** is an original research article of which as first author I was responsible for writing the entirety of the manuscript, development of the doped phantom mimicking gel, and analysis of phantom gel properties. Drs. Curtis Wiens and Chad Harris assisted with operating the MR system, as well as providing guidance and assistance with manuscript preparation and editing. Krzysztof Wawrzyn and Dr. Amgad Louka provided initial HEC gel samples and assisted in my creation of later batches of HEC gel. Drs. Will Handler and Blaine Chronik were responsible for supervision and guidance of the work.

**Chapter 3** is an original research article of which as first author I was responsible for writing the manuscript, designing the experimental set up and phantom, and analyzing the image data. Brian Dalrymple fabricated the phantom. Drs. Wiens and Harris assisted with MR operation, MR sequence optimization, and assisted with manuscript preparation. Drs. Handler and Chronik provided supervision and guidance.

**Chapter 4** is an original research article of which as first author I was responsible for writing the manuscript, collecting data, operating MR gradients, and performing data analysis. Kieffer Davieau and Dr. Eric Lessard assisted with data collection of elevator magnetic fields. Dr. Handler assisted with gradient operation and main magnet temperature data collection, along with assistance preparing initial peer reviewed research abstracts for which this work is based on. Dr. Chronik provided guidance and supervision of the work.

## Acknowledgments

A PhD is not done in a vacuum, and I would like to thank everyone who made this possible, starting with my supervisor Dr. Blaine Chronik. Thank you for providing me with the opportunity to work in such a supportive environment, where I was able to pursue projects in whichever direction they took. To the members of my advisory committee, Drs. Eugene Wong, Peter Brown, and John De Bruyn, thank you for sharing your expertise with me, you all saved me countless hours by pointing out potential pitfalls and helping focus my vision for this thesis.

To Drs. Will Handler, Curtis Wiens, and Chad Harris, thank you for the support and guidance you have all provided throughout my time here. Professionally, you have all massively contributed to my development as a scientist and through countless meetings have offered perspectives that shaped the direction of the work. It is no exaggeration to say that all these projects would be but ideas floating in the ether if it weren't for your feedback and knowledge.

In my time at Western I have been lucky to have the support of excellent technical staff, including Frank Van Sas, Brian Dalrymple, Dereck Gignac, and Krzysztof Wawrzyn, all who have been available at a moment's notice to assist with various aspects of whichever project was being conducted. Thank you for all the aid, advice, and banter throughout my time here.

To the members of the xMR Labs: Dr. Amgad Louka, Dr. Arjama Halder, Chris Brown, Dr. Eric Lessard, Kieffer Davieau, Xiao Fan Ding, John Adams, Matt McCready, and Colin Metrow. Thank you for the countless contributions to my work, both in formal collaboration and through discussions at all hours of the day. You all made this journey a wonderful experience. Thank you to my friends at Western who made it a joy to come to campus every day: Louis, James, Mark, Victor, Noah, Sandy, Mateo, Farshid, Dilanjan, Hadi, Adrien, Navid. Thank you to my friends Sarraf, Vanessa, Zamir, Tristan, Uvi, Kieran, Alex, Tim, Geoff, Colin, Taylor, Josh, Alex, Michelle, Sabrina, Kat, Tyler, and Emilee for always being there for me and keeping me sane.

Finally, thank you to my family for the endless support and encouragement in everything I have done. I couldn't do this without both of you.

# Table of Contents

Abstract.....	ii
Summary for Lay Audience.....	iii
Co-Authorship Statement.....	iv
Acknowledgments.....	v
Table of Contents.....	vi
List of Tables.....	x
List of Figures.....	xi
List of Appendices.....	xiii
List of Abbreviations.....	xiv
Chapter 1.....	1
1 Introduction.....	1
1.1 The MR System.....	2
1.1.1 Physical basis for MRI.....	3
1.1.2 The RF system.....	5
1.1.3 The Gradient System.....	6
1.2 MRI at Low Field.....	11
1.2.1 Categorization of Fields.....	11
1.2.2 Accessibility of MRI.....	13
1.2.3 Challenges of mid field MR.....	14
1.3 Thermal Mapping using MR.....	15
1.3.1 Use of Thermal Therapies.....	16
1.3.2 Modern Thermal Mapping Approaches.....	18
1.3.1 Proton Resonant Frequency.....	20
1.3.2 $T_1$ and $T_2$ .....	22

1.3.3	Apparent Diffusion Coefficient .....	24
1.3.4	Proton Density .....	25
1.4	Thesis Overview .....	26
1.5	References.....	27
Chapter 2.....		35
2	Hydroxyethylcellulose as a Tissue Mimicking Thermal Phantom Gel .....	35
2.1	Introduction.....	35
2.2	Materials and Methods.....	37
2.2.1	Phantom Production.....	37
2.2.2	T <sub>1</sub> and T <sub>2</sub> Characterization.....	38
2.2.3	Temperature Calibration Curves.....	39
2.2.4	T <sub>1</sub> Temperature Calibration .....	40
2.2.5	PRF Temperature Calibration.....	40
2.2.6	ADC Temperature Calibration.....	40
2.3	Results.....	40
2.4	Discussion.....	46
2.5	Conclusion .....	47
2.6	References.....	48
Chapter 3.....		51
3	Echo Planar Imaging Proton Resonant Frequency temperature mapping at 0.5T: Comparison to Single-Echo .....	51
3.1	Introduction.....	51
3.2	Methods.....	54
3.2.1	Phantom Production.....	54
3.2.2	Temperature-Stability Measurement .....	55
3.2.3	Temperature-Tracking Experiment.....	56

3.2.4	Temperature-Map Reconstruction .....	56
3.3	Results.....	57
3.4	Discussion.....	64
3.5	Conclusion .....	65
3.6	References.....	67
4	Challenges Facing Implementation of Thermal Mapping using MRI .....	71
4.1	Introduction.....	71
4.2	Methods.....	74
4.2.1	Measurement of magnetic field disturbances .....	74
4.2.2	Quench evaluation at variable field strengths.....	75
4.2.3	Gradient interaction measurement .....	75
4.3	Results.....	76
4.4	Discussion.....	81
4.5	Conclusion .....	84
4.6	References.....	85
5	Thesis Conclusions and Future Directions.....	87
5.1	Thesis Overview and Research Questions.....	87
5.2	Summary and Conclusions .....	87
5.3	Future Directions .....	89
5.3.1	Expanded use of doped HEC .....	90
5.3.2	Thermal mapping with Diffusion Imaging and $T_1$ .....	90
5.3.3	Further effects of mass motion and nearby construction .....	91
	Appendices.....	92
	Appendix A: Phantom Development for Comparison of Thermal Mapping .....	92
	Introduction:.....	92
	Methods:.....	93



Results:.....	94
Discussion & Conclusion:.....	98
References:.....	100
Curriculum Vitae .....	101

## List of Tables

Table 1.1: Table summarizing most common typical thermal mapping approaches [49]..... 19

Table 3.1: Parameters for the three sequences used in the temperature stability and temperature tracking tests. 22 averages were taken on the 3-slice EPI acquisition to achieve a similar update rate to the SE-GRE sequence. .... 56

Table 4.1: Summary of results of a gradient heating experiment, with fit used of  $A(1-e^{-x/\tau})$  from Figure 4.6, with time constant  $\tau$  the characteristic settling constant guiding time the magnet coils take to reach steady state. .... 81

# List of Figures

Figure 1.1: MR system at Physics and Astronomy department, Western University. Image taken by Diego Martinez..... 2

Figure 2.1: Experimental set up, with falcon tubes holding candidate solutions shown, along with the two solenoid coils used for testing and reference. .... 38

Figure 2.2:  $T_1$  and  $T_2$  relaxation times for sample mixtures of Hydroxyethyl Cellulose ..... 42

Figure 2.3:  $T_1$  relaxation time for a 3% HEC formulation..... 43

Figure 2.4: Change in Central Frequency vs Temperature ..... 44

Figure 2.5: Change in Apparent Diffusion Coefficient vs temperature..... 45

Figure 3.1: Schematic and MR scan of custom phantom ..... 58

Figure 3.2: Comparison of SE-GRE and EPI in vivo ..... 59

Figure 3.3: Photo of experimental set-up..... 60

Figure 3.4: Relative Temperature change, SE-GRE..... 61

Figure 3.5: Relative Temperature change, 3-slice EPI ..... 62

Figure 3.6: Relative Temperature change, 13-slice EPI ..... 63

Figure 4.1: Schematic of elevator probe location set up, with each spot being a measurement location..... 75

Figure 4.2: Graph of a sample time series from the passenger elevator ..... 77

Figure 4.3: Graph displaying the maximum field change due to elevators ..... 78

Figure 4.4: Set of field measurements for quenches at a series of field strengths ..... 78

Figure 4.5: Plot of the quench settling time ..... 79

Figure 4.6: Time series of magnet temperature heating .....	80
Figure A.1: Image of the prototype phantom.....	94
Figure A.2: Comparison of thermal homogenization time .....	95
Figure A.3: Structural T1 images of the phantom .....	96
Figure A.4: Thermal map comparison of the phantom.....	97

## List of Appendices

Appendix A: Phantom Development for Comparison of Thermal Mapping .....	92
---	----

## List of Abbreviations

ADC	Apparent Diffusion Coefficient
B <sub>0</sub>	Main Magnetic Field
BW	Bandwidth
CT	Computed Tomography
CuSO <sub>4</sub>	Copper (II) Sulfate
EPI	Echo Planar Imaging
FID	Free Induction Decay
GRE	Gradient Recalled Echo
HEC	Hydroxyethyl Cellulose
ISO/TS	International Organization for Standardization Technical Standard
MnCl	Manganese Chloride
MR	Magnetic Resonance
MRI	Magnetic Resonance Imaging
PD	Proton Density
PRF	Proton Resonant Frequency
RF	Radiofrequency
SE-GRE	Single Echo Gradient Recalled Echo
SNR	Signal to Noise Ratio

$T_1$	Longitudinal Relaxation Constant
$T_2$	Irreversible Transverse Relaxation Constant
$T_2^*$	Apparent Transverse Relaxation Constant
$T_c$	Superconductor Critical Temperature
TE	Echo Time
TR	Repetition Time
$\alpha$	Proton Resonant Frequency coefficient

## Chapter 1

### 1 Introduction

Magnetic Resonance Imaging (MR or MRI) is a non-invasive imaging modality that uses radiation to probe the human body [1]. In contrast to other imaging modalities such as x-ray based techniques, the lack of ionizing radiation necessary to image provides one of the biggest benefits to using MRI, as a patient could undergo limitless MR scans without increased likelihood of cancer. Along with the patient-safety benefit, MR provides excellent soft-tissue contrast and can highlight tissue properties such as elasticity, permeability, or thermal conductivity.

In large part due to the advantages of MRI, the use of the modality has seen growth globally. In Canada specifically, approximately 1 million exams were performed in 2007, and this rose to 1.86 million in 2017 [2], [3]. This corresponds to being in the lower half of MR systems compared to other reporting countries, and 69% of systems have been installed within the past 10 years as of 2017 [2]. More recently, 2022 reports indicate a 30.8% unit increase in the number of MRI units [4]. This all points to a particularly growing field in Canada, and room for growth compared to other modalities.

Alongside this are the developments in combined MR systems, such a PET-MR and MR-Linac systems, which have specialized use. In terms of PET-MR systems, as of 2017 there were no systems in clinical use, but 3 in clinical research use, pointing to further growth opportunity within the interventional medical space.

In Canada, the majority of MR systems have a main field strength of 1.5T [3], and as technology had improved, there has been a constant trend towards higher field strengths to take advantage of the linear increase in Signal-to-Noise (SNR) at higher field, culminating in the FDA approval for a 7 T scanner for clinical use in the USA in 2017 [5]. In research settings, these MR systems can have even higher field strengths, reaching up to 11.75 T [6].



Lost in this reach for higher field strength has been a look at the capabilities of modern mid-field (<1T) systems, which can take advantage of different physiological processes while reducing sample heating [7]–[10]. This thesis is focused on evaluating the abilities of such a mid-field (0.5T) MR system in measuring temperature by optimizing approaches done at higher field strength and taking advantage of the different tissue properties at this lower field strength. As well, the thesis aims to explore the challenges that face these systems when used interventionally and when placed in non-specialized environments.

## 1.1 The MR System

This research explores novel applications of MR Methods, where the benefits of different components of the MR system are leveraged to provide temperature-sensitive image contrast. For an MR system, there are three main components: the main magnet, the gradient coils, and the radiofrequency (RF) system.



**Figure 1.1:** MR system at Physics and Astronomy department, Western University. Image taken by Diego Martinez.

### 1.1.1 Physical basis for MRI

MRI relies on the principle of nuclear magnetic resonance, which refers to the behavior of nuclei in the body that has a net spin due to unpaired nucleons. Through these unpaired nucleons, the net spin can be manipulated using an external net magnetic field, which is provided by the main magnet (in clinical use this varies between 0.2 to 7 T).

If we look at a spin- $\frac{1}{2}$  particle along the direction of the magnetic field,  $z$ , the particle can be described using the states  $|+z\rangle$  and  $|-z\rangle$ , the natural eigenbasis for a measurement along  $z$ . The populations that exist in each of the states can be determined using the Hamiltonian of the interaction with the main magnetic field (called  $\mathbf{B}_0$ ) which is:

$$\hat{H} = -\hat{\mu} \cdot \mathbf{B}_0 \quad (1.1)$$

where  $\mu$  represents the magnetic moment of the spin- $\frac{1}{2}$  particle, corresponding to the spin operator  $\hat{\mathbf{S}}$  and the field  $\mathbf{B}$  applied along the  $z$  direction, giving  $B_0\mathbf{k}$ . In this representation, the energy of a spin aligned with the  $B_0$  field results in:

$$\begin{aligned} \hat{H}|+z\rangle &= -\hat{\mathbf{S}} \cdot \hat{\mathbf{B}}|+z\rangle & (1.2) \\ &= \omega_0 \hat{S}_z |+z\rangle \\ \hat{H}|+z\rangle &= -\frac{\hbar\omega_0}{2} \\ \hat{H}|-z\rangle &= \frac{\hbar\omega_0}{2} \end{aligned}$$

This difference of  $\hbar\omega_0$  in energy between the  $z$ -component in the magnetization between these two states creates a small bias in the spin- $\frac{1}{2}$  particles in the sample that initially had no net magnetization before exposure to this magnetic field. As a collective ensemble of

particles, this leads to the creation of a small net magnetization with the magnetic field. Although the spin of a single nucleus may not provide a detectable signal in a MR experiment, the net magnetization of a mole of a sample with a  $\sim 10^{23}$  spins *may* however provide enough of a net magnetization to provide a detectable signal.

This generated net magnetization is linearly proportional to the strength of the  $B_0$  field and is influenced by the Boltzmann distribution of energies in the sample. This distribution can be leveraged for image contrast and will be discussed in more detail later. The general relation between magnetization and magnetic field is called Curie's Law, and is

$$M = C \frac{B_0}{T} \quad (1.3)$$

with C representing the curie constant, a relation between the magnetic susceptibility of a material with its temperature, T. The benefits of higher field strength can be seen, as a higher field will result in more magnetization and this in turn results in more signal measured from the sample. In turn, one could further magnetize a sample by cooling down, however this would not provide significant benefit unless significant cooling was performed, something that is less preferable in vivo.

The net magnetization will precess around the direction of the magnetic field that induced the magnetization. The frequency of this precession,  $\omega_0$ , can be described using

$$\omega_0 = \gamma B_0 \quad (1.4)$$

In the case of hydrogen nuclei in water, (the most abundant source of a singular type of nuclei in the body), the gyromagnetic ratio  $\gamma$  of these hydrogen nuclei is 42.58 MHz/T,

meaning that at 1 T the hydrogen nuclei would precess with a frequency 42.58 MHz around the  $z$  axis, and at 0.5T, this precession would occur at 21.29 MHz.

This magnetization, if tipped from the direction of the main field, would precess around the main field axis, with frequency proportional to both the intrinsic properties of the nuclei and the strength of the field.

### 1.1.2 The RF system

The excitation of the magnetization is a critical element of the NMR experiment, and this process is handled by the RF system. As this is only a quick overview, a full account of this process is covered in *Magnetic resonance imaging: physical principles and sequence design* by Brown, Cheng, Haacke, Thompson, and Venkatesan [1].

Using non-superconducting coils, a modern transmit RF coil will produce a field that is perpendicular to the main magnetic field. This field does not need to be anywhere near as strong as the field from the main magnet, instead inducing a field in the  $\mu\text{T}$  range. This perpendicular field creates a torque on the magnetization, which causes it to precess around this field created by the RF system (which we call the  $B_1$  field), and thus the magnetization is tipped into the transverse plane. This process is called the excitation of spins, as the system is no longer in its lowest energy state (since it is no longer aligned with the stronger  $B_0$  field). In theory, by applying this  $B_1$  field for a given amount of time, the angle that the magnetization makes with the  $z$ -axis changes, with the relation following:

$$\theta = \int_0^T \gamma B_1 \quad (1.5)$$

By matching the frequency of rotation to the precession frequency of the nuclei being imaged, we can ensure that the  $B_1$  field is perpendicular to magnetization. This concept of

being on-resonance (matching the frequency of  $B_1$  to  $\omega_0$ ) produces the largest amount of excitation, as this means the most spins are tipped into the transverse plane.

Now, when this magnetization is in the transverse plane, there are several important mechanisms that allow it to return to the lowest energy state. The first is the interaction with the local environment, which can absorb energy as the magnetization builds back up in the longitudinal direction. This is referred to as spin-lattice relaxation, and the time constant for which this happens is called  $T_1$ . The magnetization at a given time is then:

$$M(t) = M_0(1 - e^{-\frac{t}{T_1}}) \quad (1.6)$$

These spins can also interact with one another, and this interaction causes subtle changes in the local magnetic field, even within a very small sample region. These changes in magnetic field cause the precession of individual spins to change, meaning that even without the  $T_1$  relaxation, the transverse magnetization will disperse due to these field variations (as some identical nuclei will precess faster than others). This is referred to as spin-spin relaxation and the time constant is  $T_2$ .

In a similar vein, field inhomogeneity caused by the system itself (the static field having this inhomogeneity) leads to the uneven dispersion of spins within the magnetization. This is referred to as  $T_2'$ , and mitigating its effects has been a major concern throughout the development of MR technology, culminating in the stable field that can be maintained in modern MR systems.

### 1.1.3 The Gradient System

To produce an image, it is not enough to simply record the signal, as the measured signal will only describe the total signal from the entire sample that has been excited. To localize the measured signal, it is necessary to vary the magnetic field in 3 directions which can form a basis for the sample space, typically chosen to be the orthogonal  $xyz$  basis. By

creating a spatially varying offset to the field, it is possible to identify where the signal is coming from.

This can be illustrated by considering just one of the axes, say the  $z$  axis. By creating a field gradient, the field at some position along the axis  $\mathbf{B}(z) = (B_0 + G_z z)\mathbf{k}$ . From equation (1.8) this will change the frequency at which the spins at that spatial location will precess, and this in turn means that by applying a  $B_1$  field at that particular resonant frequency, we can selectively excite the nuclei. Including the three gradients that can be produced, the overall  $B$  field (before an RF pulse):

$$\mathbf{B}(x, y, z) = \begin{bmatrix} \mathbf{0} \\ \mathbf{0} \\ B_0 + G_x x + G_y y + G_z z \end{bmatrix} \quad (1.7)$$

The gradients are produced by their own set of non-superconducting coils, normally with two layers for each direction. In an ideal world, these gradients would be turned on and off instantaneously to the required strength. Physically, Lenz Law prevents us from instantly having a maximum current flow through our system, as the change in field will induce a current opposing this change, leading to a minimum ramp time. In terms of imaging a patient, there are safety limits established for gradients limiting how quickly they can ramp up, ensuring the safety of the coils and preventing the rate of change in field within the area a patient could be in from being too high. From the Maxwell-Faraday equation in differential form, the relation between a changing magnetic field and an induced electric field:

$$\frac{\partial \mathbf{B}}{\partial t} = -\nabla \times \mathbf{E} \quad (1.8)$$

Where  $\nabla$  is the curl operator, and  $\mathbf{E}$  is the electric field. The stronger the gradient field can be produced, the larger the difference in frequency between nuclei separated by a distance  $\mathbf{r}$ . This in turn allows for the signal measured from an excitation to be better localized, as there is a smaller range of spatial region within a certain frequency range  $\Delta\omega$ .

This resolution concept relates to the phase accrued due to the gradient and introduces the concept of the spatial frequency variable  $k$ . From the equation of phase change over distance:

$$\phi(x) = 2\pi \left( \frac{\gamma}{2\pi} G_x \tau \right) x \quad (1.9)$$

$$k_x = \frac{\gamma}{2\pi} G_x \tau \quad (1.10)$$

This concept of  $k$  can be extended to the  $y$  and  $z$  axes and relates to the phase offset that we are sensitive to in any acquisition. The signal from measurement of an RF pulse from earlier can be written (for only the  $x$  direction) as:

$$S(t) \propto \int \rho(\mathbf{r}) e^{i\phi(\mathbf{r})} dV \int e^{i\omega t} S(TE, k_x) \propto \int \rho(x) e^{i2\pi k_x x} dx \quad (1.11)$$

Where TE is the echo time of the pulse sequence,  $\rho$  is the proton density. Which can be recognized as the Fourier transform equation, where the variable  $k_x$  is the variable which the spectral decomposition of the image in  $x$  is based on. Thus, this density of spins  $\rho(x)$  can be obtained through the inverse Fourier transform of the signal received as a function of  $k_x$ :

$$\rho(x) = \mathcal{F}^{-1}[S(TE, k_x)] \quad (1.12)$$

Which, as earlier can be extended to the  $y$  and  $z$  directions. Traversing  $k$ -space and collecting signal intensities thus allows us to determine the density of nuclei and create an image using the inverse 2D or 3D Fourier transforms.

The sequential combination of RF pulses and application of gradients results in what is called a pulse sequence, where the timing of each is ordered to produce a different weighting of images. In the simplest case, by applying an RF pulse to excite the nuclei and immediately recording the signal collected (using the gradients to encode the location), the resulting image will be a slab of signal that has been collected, from which the frequencies can be used to generate the image. From this, the intensity of each voxel produces the magnitude in the greyscale image.

In the development of MR methods, different combinations of use of gradients and the RF system have been created to leverage these behaviors of nuclei and measure the contrast of not just hydrogen, but also other agents in the body.

### 1.1.3.1 Gradient Recalled Echo and Echo Planar Imaging

In MR there are multiple ways to combine RF excitations and gradient pulses to manipulate protons and obtain the collection of spatial frequencies in  $k$ -space which give



information about the phase of spins, which are then used to form an image. In the scope of this work, both gradient recalled echo, and echo planar imaging are used to acquire phase information.

Gradient echo produces a signal at a set echo time (TE) by applying a dephasing gradient lobe after the RF excitation has been performed. Subsequently, a lobe in the opposite direction is applied (over a longer period, but at lower gradient strength). The point at which the total area of the applied refocusing lobe matches the area of the dephasing lobe, a moment of maximum magnetization is formed, called an echo, which has signal which has decayed with time constant  $T_2^*$ . As the gradient refocuses the echo, signal can be acquired along a line of k-space, with this process repeated and lines of k-space collected until sufficient k-space information can be used to form an image with magnitude and phase information. Images can be collected using a single echo per RF excitation (called single echo gradient recalled echo, or SE-GRE), or with multiple echoes collected for a single excitation which are then combined [11].

The straightforward nature of GRE approaches makes it a common one in practice, however the drawback of collecting only one line of k-space per repetition time makes it potentially too slow for applications where temporal resolution is a priority. To this end, Echo Planar Imaging (EPI), offers the benefit of collecting an entire plane of k-space data in a single excitation, as opposed to just one line. This is achieved by applying a small phase encoding gradient pulse between frequency encoding lines, such that the overall echo is acquired at the origin of k-space, while samples are taken in a raster fashion [1]. The actual number of k-space lines collected in every shot is referred to as the Echo Train Length, with single shot referring to a complete coverage of k-space and multi shot referring to multiple excitations being done over a traversal of k-space [12]. Although it allows for fast imaging overall, the approach is susceptible to blurring in the phase encode direction, as this is acquired much more slowly (in small blips) as opposed to the frequency encoded direction. Nonetheless, the benefits in acquisition time are significant compared to a SE-GRE approach [13].

## 1.2 MRI at Low Field

### 1.2.1 Categorization of Fields

As the proliferation of MR has occurred throughout the world, research and development has led to an increase in the field strengths and as mentioned, stability of these systems.

Along with this development, multiple conventions for categorizing fields have emerged. A common categorization is into the following four: “low-field” for static field strengths up to 0.1 T, “mid-field” for field strengths up to 1 T, “high-field” for fields between 1 T and 7 T, and “ultra high-field” for anything at or above 7 T. These categories are all a bit arbitrary and up for interpretation, but it is a grouping which can be distinguished by the capabilities at each field strength.

As of 2020, ultra high-field MRI is used only in research capabilities, where the field strength allows for high-quality functional MRI, very good signal to noise ratio (SNR) (generally due to the larger magnetization induced, which translates to signal received through the RF coils), and good ability to conduct MR spectroscopy. This high field comes with drawbacks: worse patient experience compared to lower field (particularly dizziness during the scan process) [14], amplified  $B_0$  and  $B_1$  inhomogeneities, and the dielectric effect producing artefacts, limiting the potential image quality [15]. As well, with an average cost in 2015 of 10 million dollars for a 7 T system installed [16], the high cost of these systems is a factor limiting widespread adoption.

High-field systems, particularly 1.5 T and 3 T systems are generally the ones that are used in a clinical setting [3], and provide many of the benefits that also occur at ultra high field. This includes also having good SNR, producing good quality for standard imaging techniques, and allowing for Diffusion Imaging along with Diffusion Tensor Imaging. These systems still contain heating concerns, with harder limits on the strength that the RF pulses can be compared to low field systems, particularly when imaging patients with implants[17]–[19].

Modern mid- and low-field systems, with advanced gradients and magnet design, can provide comparable quality  $T_1$  imaging as higher field counterparts due to the ability to run gradients more strongly while staying within regulatory limits. These systems are relatively low cost, and (due to the lower field) can provide a benefit in lung imaging due to reduced susceptibility artefacts[7], [9]. Overall, these systems are limited by the reduction in SNR, and this limits some of the modern imaging techniques from being conducted as there are question as to if there is enough signal to accurately implement.

This renewed commercial interest has led to a number of new entries in the world of mid- and low-field MR intended for human application, particularly in the last 5 years. These include but are not limited to the 64 mT Hyperfine Swoop head scanner, the 66 mT Promaxo scanner, the 0.55 T Siemens Magnetom Free.Max, and the scanner used in parts of this work, the 0.5 T Synaptive EVERY scanner. Additionally, there have been use cases where magnets initially designed to operate  $>1$  T have been ramped down and operated at 0.55 T, particularly the 1.5 T Siemens Aera scanner.

Many of these systems come with the additional feature of being what is called “cryogen-free”, which means that in the windings of the main magnet producing the main static magnetic field are not required to be immersed in cryogen to maintain superconductivity. Instead, these systems use a closed heat-sink system to extract heat from the windings and maintain the magnet below the critical temperature at which superconductivity begins.

Typically in the case of an emergency, MR systems have mechanisms in place that can vent out the cryogen which typically immerses the main magnet windings. This allows the superconducting coils to heat up above a critical temperature ( $T_c$ ) at which point they become non-superconducting. This is necessary for emergency response teams to safely approach the bore of the magnet in emergency situations [20]. The cryogen that is boiled off in this scenario must be removed from the MR suite, and the installation of these systems is another cost associated with a typical MR scanner.

In both cryogen and cryogen-free systems, heater elements help to achieve the creation of a non-superconducting region in the main magnet windings. This region, which now has a resistance will heat, which propagates this non-superconducting region, and thus can quickly make the entire magnet non-superconducting [21], [22]. In these cases, quench-protection systems are put in place to protect the MR components from damage during these emergency situations and are designed to operate at the field strength the magnet is built for, necessitating investigation into the quench behavior for magnets which are run at field strengths they were not designed for.

### 1.2.2 Accessibility of MRI

Along with some of the tissue parameters and sample heating benefits of performing MRI in the mid-field strengths, the accessibility of these systems to the general population is a strong motivating factor in the adoption of these systems. All MR magnets have magnetic fields that extend beyond the bore of the magnet, even with windings in the main magnet called shield coils that are meant to reduce the reach of the magnetic field of the system outside the bore of the magnet. These fields, called fringe fields, limit how close operators and technicians can come to the magnet, and require an organized blueprint that considers several safety measures including access protocols, room zoning, and safety training for operators and clinicians.

Due to the need for specialized infrastructure near an MR system, these cannot generally be installed in any generic environment that may not adequately protect the magnet from the common ferromagnetic building elements and won't have the specialized safety systems integrated that are required for MRI use. Typically, there is a "4-zone" architecture which keeps general populations in regions 1 and 2, with a restricted access to the console room (zone 3), and a shielded room with the MR system itself (Zone 4) [23]. These architectures ensure that only vetted patients can be near an MR system, while isolating the magnet from its environment. Other common safety measures include but are not limited to RF shielding in the magnet room, emergency shut-off buttons, pre-magnet waiting rooms, locked access to the magnet, and special compartments for metallic objects.

As with all systems, implementing safety features brings cost, which limits the widespread use of such a strong magnet. As stated, with a rough price of \$10 million for the most modern 7 T systems without accounting for the specialized rooming that is required, lesser funded clinics and smaller doctors' offices cannot accommodate such a high cost and high maintenance systems, which leaves hospitals as the primary customers of MRI systems[3].

Alleviating some of these pressures is the rise in modern mid-field systems, both in original design 0.5 T systems, and in the re-purposing of higher field MR systems to run at this reduced field [7]. Due to the lower static field, the fringe fields can be made to extend far less beyond the bore of the magnet, especially with a well optimized active shield. This opens the opportunity to forego the typical MR architecture used to isolate the MR system from its surroundings and place these systems in less specialized environments. This in turn reduces the siting costs and means that, along with the cost of the system itself, more care centers can be outfitted with an MR system.

### 1.2.3 Challenges of mid field MR

Although mid-field MR systems can leverage many beneficial qualities of the lowered susceptibility artefacts and reduced sample heating, there are negative considerations in image quality that are considered, as addressed earlier. Alongside this, there are other secondary issues that need to be addressed with the specific siting of the magnets outside of specialized rooms in the pursuit of improving the accessibility to the general population.

As a consequence of developing accessible lower field MR systems, these can be placed much nearer to building elements which can adversely affect the stability of the main magnetic field used in the imaging process. This can negatively affect image quality and device localization [24], as a changing local magnetic environment produces artifacts and limits the ability to delineate regions of interest in images taken using the system. For example, in imaging sequences that attempt to categorize the density of different molecules in a sample (proton density weighted imaging, one of the three main imaging contrasts along with  $T_1$  and  $T_2$ ), a main magnetic field that does not significantly vary with time is

required [25]. As a function of both using a lower field system with lower SNR to higher field counterparts and the placement of this system in non-specialized environment, the development of more accessible MRI has especially difficult optimization challenges to overcome in providing high quality images. This is however the risk that occurs when there are potentially magnetic elements in the vicinity of the magnetic system.

### 1.3 Thermal Mapping using MR

The temperature of a sample in an MRI system is critically important, to the point where one of the first relations that a student learning about NMR will learn is the relation between net magnetization and temperature, called Curie's Law [1]:

$$M_0 \propto \frac{B_0}{T} \quad (1.13)$$

This simplified relation highlights how for any sample, the signal received by the RF coil will change based on the temperature of the sample. This simply shows that on a fundamental level it is possible to use the signal received from MRI to measure the temperature inside the body, at the very least in the form of a change in signal from a region of sample over time.

In turn, this provides a very useful opportunity, as it is not possible to measure the temperature in the human body using any other non-invasive method. Effective applications of thermal mapping (sometimes referred to as thermometry or thermography) can produce localized images of temperature and display the temperatures as a map over an MRI scan, either as a single measurement or a time-series monitoring of relative change in temperature in a region of the body [25].

Furthermore, the development of thermometry techniques have been of particular interest to the medical community in monitoring hyperthermia or cryotherapy. Being able to accurately measure the dose applied to a patient being treated using these treatments is critical to reaching successful medical endpoints [26].

### 1.3.1 Use of Thermal Therapies

Thermal therapies have found significant use within the medical community, including treatments in breast, bone, liver, and even brain tumors [27]–[30] along with treatment of uterine fibroids and movement disorders such as Parkinson's tremor [31]. In these applications, some which would normally be treated using chemotherapy, the use of a well monitored thermal therapy has shown value as an additional treatment with established value.

In the cases where these approaches heat tissue above an index temperature for a set amount time, there have been established methods for accurately predicting cellular necrosis and effectively control tumors [26], [32]. As such, improving and expanding this field continued to grow and has become a routine component of patient care, with many minimally invasive modalities of ablation developed [32]. These include Radio Frequency, Microwave, laser, and High Intensity Focused Ultrasound (HIFU) methodologies which work to heat tissue above  $\sim 60^\circ\text{C}$  in order to reach cytotoxic levels [33]. This technique offers several advantages, including a reduced risk of complications, shorter recovery time, and potential for outpatient treatment, making it a valuable alternative to invasive traditional surgical interventions. There also exist lower strength hyperthermia treatments where tissue is heated up in the range of  $\sim 50^\circ\text{C}$  with treatment times in the minutes to hours, while high temperature hyperthermia can reach temperatures far beyond this for shorter treatment times.

Cold therapy, also called cryotherapy, utilizes cold temperatures through ice packs, cold compresses, or specialized chambers to constrict blood vessels, reduce inflammation, and numb nerve endings [34], [35]. Hypoxic-Ischemic Encephalopathy is an example of this

cryotherapy, where treatments can either involve cooling of an infant head or entire body to target temperatures of 34.5°C and 33.5°C respectively[36]. At the conclusion of the treatment, infants are re-warmed over the span of 6 to 12 hours, at a rate of 0.5°C/hour. The benefit in these heating and cooling treatment methods is the non-invasive nature, which can reduce patient contact and minimize complications.

In most hyperthermia treatments, there is a system which generates the source of heating, and there is a needle/focusing device that delivers this generated energy to the tissue [18]. Depending on the location of the treatment area, there are a various monitoring mechanisms for the application of the thermal therapy, and circumstances which guide which method is ideal [37]–[41].

Of modern interest has been the non-invasive nature of HIFU as a treatment option. With a standard ultrasound using energies of around 720 mW/cm<sup>2</sup>, High Intensity Focused Ultrasound uses intensities orders of magnitude higher (100-10,000 W/cm<sup>2</sup>). These acoustic waves can be manipulated to accurately deposit energy in a region of interest, leading to remote heating. The waves produce both thermal and mechanical damage, which leads to the ability to combine the treatment with targeted drug delivery by drug-containing micro-bubbles [42].

With such promising benefits, there are significant limitations to the use of HIFU. There is a limit to the depth that ultrasound can penetrate within the body. As well, due to different densities of tissue and bone in the body, there is risk of damage to nearby body elements such as peripheral nerves and skin. As with MR scans, there is a risk of patient movement affecting the delineation or targeted region in the treatment, so application of HIFU near the lungs is difficult to conduct [42]. As with all potential treatments, HIFU needs to be carefully planned to minimize the risks to patient safety and optimize the treatment effects, with this method still providing a very tempting option for treatment due to the fully non-invasive nature [41].



Ensuring the correct thermal dose delivery is critical in treatment planning and execution. For this reason, work has focused on how to integrate thermometry into these applications, with results showing safety concerns and impracticality for invasive thermometry methods [43]. To this end, the development of non-invasive thermal mapping was quickly identified as a promising approach and has grown in relevance alongside the growth in MR capability.

As early as 1998, there has been research use of thermometry techniques using MR systems for the purposes of monitoring and modelling the cell death in an ablated region [44], [45]. As MR systems have continued to develop, there has been an expansion in the number of methods which can be used to create these thermal maps. Today, the most common methods can generate relative temperature maps, with some research methods able to produce absolute temperatures, and the outlook for future development being the development of robust absolute temperature measurement.

Integration of MR guidance to HIFU has grown since initial development [46]. An MRI scan can be used to visualize and plan treatment, and it can also guide the application of the focused ultrasound [47]. These approaches are specifically tailored to maximize the SNR and use high volume RF coils to avoid interference between the RF array elements and the HIFU system [48], along with multi-channel RF approaches to improve the SNR.

### 1.3.2 Modern Thermal Mapping Approaches

Multiple approaches to thermal mapping have been developed, each with benefits and concerns based on the manipulation of nuclear spins in the imaged sample. Particularly important is the relation with the main magnetic field, as different imaging techniques will respond differently say at 3 T vs 1.5 T. The generally accepted standard technique for thermometry is using what's called the proton resonant frequency (PRF) shift, with variations on the method to offer some optimal SNR [49], [50]. Alongside this method, important consideration at low field should be taken to proton density (PD) imaging, Diffusion imaging, and  $T_1/T_2$  weighted imaging, an overview of which can be seen in **Table 1.1**.

<b>Method</b>	<b>Mechanism</b>	<b>Pros</b>	<b>Cons</b>	<b>B<sub>0</sub> Dependence</b>
Proton resonant frequency	Temperature dependence of hydrogen bonds	High spatiotemporal resolution, linear function of temperature	Does not work in Adipose tissue due to lack of water molecules	Linear increase
T <sub>1</sub>	Energy exchange rate in sample increases with temperature	Readily available and common, can be used in all tissue types	Low temperature sensitivity; non-linear change at high temp	T <sub>1</sub> increases with B <sub>0</sub> , but observed T <sub>1</sub> contrast decreases
Proton Density	Proton polarization density is inversely proportional to tissue temperature	Relatively independent of tissue type, also very common	Very low sensitivity (~0.3%/°C)	PD increases linearly with field, but sensitivity unaffected
Diffusion	Molecular diffusion obeys Stokes-Einstein relation between temperature and diffusion coefficient, $D$	Readily available and common	Slow to image, sensitive to motion	Negligible

**Table 1.1:** Table summarizing most common typical thermal mapping approaches [49]

### 1.3.3 Proton Resonant Frequency

#### 1.3.3.1 Basics

As stated, measuring the shift of the proton resonant frequency in water is the most pervasive method for measuring temperature, and thus is the first stop when trying to create temperature maps. The method hinges on the slight variations in the magnetic field that is experienced in water molecules, shown as [51], [52] (where  $\sigma$  is the phase shift):

$$\begin{aligned} B_{loc} &= B_0 - B_0\sigma \\ B_{loc} &= (1 - \sigma)B_0 \end{aligned} \tag{1.14}$$

This varied field changes the frequency with which the hydrogen nuclei precesses, as described by the Larmor frequency  $\omega_{loc} = \gamma B_{loc}$ . Thus, should the variations in field be temperature dependent, this can be observed.

Hydrogen nuclei in water are less insulated from the macroscopic field when hydrogen bonds are formed with doping agents, water molecules, or other molecules. As temperature increases these bonds become stretched or broken; this causes the water molecules to spend less time in a bond, and this means the average screening of the  $^1\text{H}$  is increased. The temperature dependence of the screening constant is linear, giving:

$$\sigma_T(T) = \alpha T \tag{1.15}$$

with  $\alpha \approx -0.01$  ppm per degree, depending on exact tissue [49]. A drawback of this method is the reliance on aqueous tissue to generate a detectable shift. In adipose tissue, the shift

in local field is governed much more by the susceptibility of the tissue and thus other methods are required for temperature measurement.

### 1.3.3.2 Phase Imaging

When implementing PRF, there is some variation in approach which brings benefits and drawbacks. One of these approaches is called spectroscopic imaging. In this method, the MR spectrum is acquired, and the water peak is compared to a reference peak (lipid or other) to calculate the variation. With a reference water peak, the absolute temperature can be measured in this way as well. However, this method requires multiple time points so that the frequency information can be extracted. This makes the process slower and more susceptible to movements of organs and requires more data to be acquired [52].

In contrast, the use of phase temperature imaging uses a single echo time (TE) value and this reduces the data requirements while giving better spatial resolution. The drawback being that there is more susceptibility to unrelated field variation [53]. Using a gradient recalled echo (GRE) sequence, the phase change between a baseline image and a subsequent image can be calculated, and the relationship with temperature shown as:

$$\Delta T(t) = \frac{\Phi(t) - \Phi_0}{\gamma \alpha B_0 \cdot TE} \quad (1.16)$$

where  $\Phi(t)$  is the phase at a certain time and  $\Phi_0$  is the baseline phase measurement. In the case where this baseline temperature is also known, we can determine the absolute temperature of the system. This equation underpins much of the work in this thesis, as by measuring the phase utilized in various methods as will be seen in Chapter 3, we can measure the change in temperature based on this equation. As well the measured phase uncertainty can be converted to an uncertainty in temperature measurement following this relation as well.

Due to the  $B_0^{-1}$  term, the contrast using this method improves at lower field strengths, however, the common methods of acquiring PRF such as spatial-spectral (SPSP) pulse sequences or fat suppression pulses becomes difficult at low field strength due to the small offset of fat relative to water. Regardless, phase mapping is the most widespread implementation of PRF [54].

### 1.3.4 $T_1$ and $T_2$

Introduced earlier,  $T_1$  relaxation represents the interaction between the surrounding lattice and the proton spins. One way to describe the temperature dependence of the  $T_1$  time can be given by:

$$T_1 \propto e^{-\frac{E_a}{kT}} \quad (1.17)$$

with  $E_a$  the activation energy of the relaxation,  $k$  being the Boltzmann Constant, and  $T$  the temperature of the sample. These measures give a range of temperature dependence between 1-2%/°C depending on the tissue [55], and lead to multiple  $T_1$  images taken over time as a method for measuring relative change in temperature [56].

For signal received from the RF coils, the signal equation based on the flip angle and the Magnetization is [57]:

$$S = M_0 \sin(\alpha) \frac{1 - E_1}{1 - \cos(\alpha)E_1} \quad (1.18)$$

It is important to note that the magnetization is also temperature dependent, and  $E_1$  is the term that contains the temperature-shift effects from the temperature, given as:

(1.19)

$$E_1 = e^{-\frac{TR}{T_1(T_{ref} + m(T - T_{ref}))}}$$

Where TR is the repetition time of the pulse sequence,  $T_1$  is the spin lattice relaxation time,  $T_{ref}$  is the reference temperature, and T is the measured temperature. From the signal equation, there are benefits in SNR by increasing the field strength ( $M_0$  increase), however as previously covered the  $T_1$  value itself increases with field strength, leading to better contrast itself at lower field [49]. Previous studies have shown a 1-2% change in  $T_1$  time per degree Celsius[57], with  $T_1$  increasing with temperature. This opens the opportunity for better SNR consideration making  $T_1$  a promising opportunity at low field.

The benefit of the commonality of  $T_1$  imaging is the well-developed methods for quickly acquiring these images, and the fast nature of acquisition reduces the effect of motion within a possible patient.

The other main relaxation mechanism, called spin-spin relaxation and with time constant  $T_2$ , also has a temperature dependence as the higher temperature causes more random thermal motions. This interaction causes variations in the local field over time and will dephase net magnetization with  $\omega_{loc} = \gamma B_{loc}$ . One benefit is that, since the relaxation is based on the interactions between spins, the field strength at which the experiment is carried out doesn't change the  $T_2$  time. Just as with  $T_1$ , the relationship with temperature can be described

(1.20)

$$\frac{1}{T_2} = \omega_{loc}^2 \left( \tau_c + \frac{\tau_c}{1 + \omega_0^2 \tau_c^2} \right)$$

where  $\tau_c$  represents the correlation time in the spin-spin interaction,  $\omega_{loc}$  represents the local rotational frequency, and  $\omega_0$  is the baseline frequency. As temperature increases, the time constant decreases, as  $\tau_c \propto \frac{1}{T}$ , and leads to an overall increase in  $T_2$ , so both  $T_1$  and  $T_2$  increase with temperature.

The temperature dependence of  $T_2$  imaging has been known for as long as  $T_1$ , however due to very slow spin echo-based methods generally needed to acquire  $T_2$  images, the method has not gained nearly the same popularity [49]. However, work has shown that the change in  $T_2$  is both linearly dependent on temperature and has a sensitivity of about 5-7ms/ $^{\circ}$  C depending on the tissue [56], which offers benefits in sensitivity over some other methods. Recently, by using modern readout methods for spin echo imaging, a scan time of 15-16 seconds per image has been achieved [58], compared with the  $T_1$  time of about 9 seconds per image [59].

### 1.3.5 Apparent Diffusion Coefficient

A measure of temperature can be obtained through the measurement of molecular diffusion in tissue, based on the Arrhenius relation between baseline diffusion and the translational self-diffusion coefficient, with

$$D \approx D_0 e^{-E_a(D)/kT} \quad (1.21)$$

Where we have  $D_0$  as the baseline diffusion,  $E_a$  the activation energy for this diffusion,  $k$  the Boltzmann constant, and  $T$  the absolute temperature in the sample. To acquire the diffusion measure, strong gradients are applied before excitation, causing spins moving in the direction of the gradient to experience dispersion, while stationary spins do not. This net signal loss is related to the dispersion of spins, and by measuring this in each voxel, a map of diffusion coefficients can be made. However, since the measured diffusion can be altered by the cellular structures, boundaries and tissue perfusion, these

measurements are called the apparent diffusion coefficient (ADC) [49]. Measuring the change in ADC over temperature, a temperature coefficient for ADC can be established and used for thermal mapping.

### 1.3.6 Apparent Proton Density

From the definition of Curie's Law stated earlier, it is suggested that there is an inverse relation between the magnetization and the temperature of a sample. In the case of apparent proton density imaging, this relationship is used to directly measure temperature, simply by taking an MR scan with a short echo time and long repetition time, the relative density of protons in the voxels of an image can be determined [60]. As proton density is proportional to the equilibrium nuclear magnetization, the signal relationship becomes [40]:

$$PD = \frac{N\gamma^2\hbar^2s(s+1)B_0}{3kT} \quad (1.22)$$

where  $N$  is the density of nuclear spins,  $s$  is the nuclear spin, and  $T$  is the temperature of the sample.

The benefit of measuring temperature using this method is the lack of need for a frequency shift as is needed for PRF, something which adipose tissue does not exhibit due to its lack of water pools. This allows for the expansion of the temperature into any type of tissue, such as the breast which does not have liquid pools to measure from [61]. Due to the common nature of the pulse sequence, all that is needed is a simple spin echo sequence with a variation in echo time. From this, the apparent PD can be determined using ratios of signal from the two time points:



$$APD \sim S(TE = 0) = S(TE = T_a) \times \left( \frac{S(TE = T_b)}{S(TE = T_a)} \right)^{-\frac{T_a}{T_b - T_a}} \quad (1.23)$$

where  $T_a$  and  $T_b$  are two selected echo times that can then be used to determine temperature due to the different levels of signal at different time points. Trials on a 0.5 T system have shown a sensitivity of around 0.56%/°C [61], with a poor standard deviation of approximately 3°C. Although experiments using this method for pure thermometry have been few, there is promise for improvements with better specialized RF coils and SNR optimization, particularly for a low-field approach.

## 1.4 Thesis Overview

This thesis outlines work done to answer an initial research question “*How well can we perform thermal mapping on a 0.5 T MR system?*” which then evolved into a larger exploration of how to go about testing thermal mapping abilities, and what the implications are for using these MR systems in non-specialized locations where interference and other effects come into play. Chapter 2 begins this by developing a novel phantom gel which can be used for testing the thermal mapping that we aim to explore as the need for a step beyond doped water became evident in early studies. Chapter 3 then continues this into actual experimentation with temperature mapping and tracking, by creating a phantom with the developed gel. The temperature precision we can reach in vivo on a 0.5 T system was evaluated, along with the ability to track temperatures in the phantom while cooling. Chapter 4 then offers a series of investigations into the potential concerns with accessible MR systems, including quench behaviours on ramped-down MR systems, risks of magnet heating due to operation of strong gradients, and importantly a look into the effects of ferromagnetic object motion near an MR system. Finally, Chapter 5 outlines the significance of the work and discusses the potential future avenues.

## 1.5 References

- [1] R. W. Brown, Y.-C. N. Cheng, E. M. Haacke, M. R. Thompson, and R. Venkatesan, *Magnetic Resonance Imaging: physical principles and sequence design*. John Wiley & Sons, 2014.
- [2] Canadian Agency for Drugs in Health & Technologies, “The Canadian Medical Imaging Inventory, 2017.” 2018. [Online]. Available: [https://cadth.ca/sites/default/files/pdf/canadian\\_medical\\_imaging\\_inventory\\_2017.pdf](https://cadth.ca/sites/default/files/pdf/canadian_medical_imaging_inventory_2017.pdf)
- [3] Canadian Agency for Drugs and Technologies in Health, “Executive Summary – CMII 2019-2020 | CADTH.,” <https://www.cadth.ca/executive-summary-cmii-2019-2020>.
- [4] Canadian Agency for Drugs and Technologies in Health, “Executive Summary – CMII 2022-23 | CADTH.,” 2023.
- [5] S. Caccomo, “FDA clears first 7T magnetic resonance imaging device.” 2017. [Online]. Available: <https://www.fda.gov/news-events/press-announcements/fda-clears-first-7t-magnetic-resonance-imaging-device>
- [6] N. Savage, “The world’s most powerful MRI takes shape,” *IEEE Spectr*, vol. 50, no. 11, pp. 11–12, Nov. 2013, doi: 10.1109/MSPEC.2013.6655823.
- [7] A. E. Campbell-Washburn *et al.*, “Opportunities in interventional and diagnostic imaging by using high-performance low-field-strength MRI,” *Radiology*, vol. 293, no. 2, pp. 384–393, Oct. 2019, doi: 10.1148/RADIOL.2019190452/ASSET/IMAGES/LARGE/RADIOL.2019190452.FIG4.JPEG.
- [8] I. R. Connell, A. Panther, and B. A. Chronik, “Specific Absorption Rate in Head-Only Mid-Field Scanner: Comparisons to 1.5 T and 3 T,” in *Proc Intl Soc Mag Reson Med*, 2019, p. 4167.

- [9] J. A. Stainsby *et al.*, “Imaging at 0.5 T with high-performance system components,” *Proc 27th Annu Meet ISMRM Montr Canada*, 2019.
- [10] C. T. Harris, A. T. Curtis, I. R. Connell, P. J. Beatty, J. A. Stainsby, and C. N. Wiens, “2D Imaging near Metallic Implants at 0.5T using High Time-Bandwidth Product RF pulses,” in *ISMRM 27th Annual Proceedings*, Montreal, 2019.
- [11] H. Odéen and D. L. Parker, “Improved MR thermometry for laser interstitial thermotherapy,” *Lasers Surg Med*, vol. 51, no. 3, pp. 286–300, Mar. 2019, doi: 10.1002/LSM.23049.
- [12] R. J. Stafford, R. E. Price, C. J. Diederich, M. Kangasniemi, L. E. Olsson, and J. D. Hazle, “Interleaved echo-planar imaging for fast multiplanar magnetic resonance temperature imaging of ultrasound thermal ablation therapy,” *Journal of Magnetic Resonance Imaging*, vol. 20, no. 4, pp. 706–714, Oct. 2004, doi: 10.1002/jmri.20157.
- [13] A. Cernicanu, M. Lepetit-Coiffe, J. Roland, C. D. Becker, and S. Terraz, “Validation of fast MR thermometry at 1.5 T with gradient-echo echo planar imaging sequences: phantom and clinical feasibility studies,” *NMR Biomed*, vol. 21, no. 8, pp. 849–858, Oct. 2008, doi: 10.1002/NBM.1267.
- [14] M. J. P. van Osch and A. G. Webb, “Safety of Ultra-High Field MRI: What are the Specific Risks?,” *Curr Radiol Rep*, vol. 2, no. 8, pp. 1–8, Aug. 2014, doi: 10.1007/S40134-014-0061-0/METRICS.
- [15] M. I. Karamat, S. Darvish-Molla, and A. Santos-Diaz, “Opportunities and Challenges of 7 Tesla Magnetic Resonance Imaging: A Review,” *Critical Reviews & Trade in Biomedical Engineering*, vol. 44, no. 1–2, pp. 73–89, 2016, doi: 10.1615/CRITREVBIOEMEDENG.2016016365.
- [16] P. Balchandani and T. P. Naidich, “Ultra-high-field MR neuroimaging,” *American Journal of Neuroradiology*, vol. 36, no. 7, pp. 1204–1215, 2015.

- [17] S. N. Sarkar *et al.*, “Three-dimensional brain MRI for DBS patients within ultra-low radiofrequency power limits,” *Movement Disorders*, vol. 29, no. 4, pp. 546–549, 2014, doi: 10.1002/mds.25808.
- [18] M. Tagliati, J. Jankovic, F. Pagan, F. Susatia, I. U. Isaias, and M. S. Okun, “Safety of MRI in patients with implanted deep brain stimulation devices,” *Neuroimage*, vol. 47, no. SUPPL. 2, pp. T53-57, Aug. 2009, doi: 10.1016/j.neuroimage.2009.04.044.
- [19] A. J. Martin, “MRI in patients with deep brain stimulation electrodes: Balancing risks and benefits,” *Radiology*, vol. 293, no. 1, pp. 184–185, Aug. 2019, doi: 10.1148/RADIOL.2019191558/ASSET/IMAGES/LARGE/RADIOL.2019191558.FIG1.JPEG.
- [20] J. Kellogg, “Confronting challenges to urban-based MRI facilities,” *DOT Medbusiness News*, Mar. 2011.
- [21] K. Seo, M. Morita, S. Nakamura, T. Yamada, and Y. Jizo, “Minimum quench energy measurement for superconducting wires,” *IEEE Trans Magn*, vol. 32, no. 4 PART 2, pp. 3089–3093, 1996, doi: 10.1109/20.511529.
- [22] F. Trillaud, F. Ayela, A. Devred, and P. Tixador, “Investigation of the stability of Cu/NbTi multifilament composite wires,” *IEEE Transactions on Applied Superconductivity*, vol. 16, no. 2, pp. 1712–1716, Jun. 2006, doi: 10.1109/TASC.2006.870006.
- [23] D. Grainger, “Safety Guidelines for Magnetic Resonance Imaging Equipment in Clinical Use,” *Medicines and Healthcare Products Regulatory Agency*, pp. 1–85, 2014.
- [24] J. Cepek, B. A. Chronik, and A. Fenster, “The effects of magnetic field distortion on the accuracy of passive device localization frames in MR imaging,” *Med Phys*, vol. 41, no. 5, p. 052301, May 2014, doi: 10.1118/1.4870961.

- [25] L. Winter *et al.*, “Magnetic resonance thermometry: Methodology, pitfalls and practical solutions,” *International Journal of Hyperthermia*, vol. 32, no. 1, pp. 63–75, Jan. 2015, doi: 10.3109/02656736.2015.1108462.
- [26] K. A. Leopold *et al.*, “Cumulative minutes with T90 greater than tempindex is predictive of response of superficial malignancies to hyperthermia and radiation,” *International Journal of Radiation Oncology\*Biology\*Physics*, vol. 25, no. 5, pp. 841–847, Apr. 1993, doi: 10.1016/0360-3016(93)90314-L.
- [27] P. Wust *et al.*, “Hyperthermia in combined treatment of cancer,” *Lancet Oncology*, vol. 3, no. 8, pp. 487–497, Aug. 2002, doi: 10.1016/S1470-2045(02)00818-5.
- [28] G. C. Van Rhooon and P. Wust, “Introduction: Non-invasive thermometry for thermotherapy,” *International Journal of Hyperthermia*, vol. 21, no. 6, pp. 489–495, Sep. 2005, doi: 10.1080/02656730500272963.
- [29] A. Kickhefel, C. Weiss, J. Roland, P. Gross, F. Schick, and R. Salomir, “Correction of susceptibility-induced GRE phase shift for accurate PRFS thermometry proximal to cryoablation iceball,” *Magnetic Resonance Materials in Physics, Biology and Medicine*, vol. 25, no. 1, pp. 23–31, Feb. 2012, doi: 10.1007/S10334-011-0277-4/METRICS.
- [30] F. A. Jolesz and N. J. McDannold, “MRI-guided focused ultrasound,” in *Intraoperative Imaging and Image-Guided Therapy*, Springer, 2014, pp. 403–412.
- [31] P. Ghanouni *et al.*, “Transcranial MR-Guided Focused Ultrasound: A Review of the Technology and Neuro Applications,” *AJR Am J Roentgenol*, vol. 205, no. 1, p. 150, Jul. 2015, doi: 10.2214/AJR.14.13632.
- [32] J. R. Oleson, M. W. Dewhirst, J. M. Harrelson, K. A. Leopold, T. V. Samulski, and C. Y. Tso, “Tumor temperature distributions predict hyperthermia effect,” *International Journal of Radiation Oncology\*Biology\*Physics*, vol. 16, no. 3, pp. 559–570, Mar. 1989, doi: 10.1016/0360-3016(89)90472-0.

- [33] M. Nikfarjam, V. Muralidharan, and C. Christophi, “Mechanisms of Focal Heat Destruction of Liver Tumors,” *Journal of Surgical Research*, vol. 127, no. 2, pp. 208–223, Aug. 2005, doi: 10.1016/J.JSS.2005.02.009.
- [34] A. Peliowski-Davidovich, C. P. Society, and F. and N. Committee, “Hypothermia for newborns with hypoxic ischemic encephalopathy,” *Paediatr Child Health*, vol. 17, no. 1, pp. 41–43, Jan. 2012, doi: 10.1093/PCH/17.1.41.
- [35] M. A. Tagin, C. G. Woolcott, M. J. Vincer, R. K. Whyte, and D. A. Stinson, “Hypothermia for Neonatal Hypoxic Ischemic Encephalopathy: An Updated Systematic Review and Meta-analysis,” *Arch Pediatr Adolesc Med*, vol. 166, no. 6, pp. 558–566, Jun. 2012, doi: 10.1001/ARCHPEDIATRICS.2011.1772.
- [36] B. Lemyre and V. Chau, “Hypothermia for newborns with hypoxic-ischemic encephalopathy,” *Paediatr Child Health*, vol. 23, no. 4, pp. 285–291, Jun. 2018, doi: 10.1093/PCH/PXY028.
- [37] T. Livraghi *et al.*, “Sustained complete response and complications rates after radiofrequency ablation of very early hepatocellular carcinoma in cirrhosis: Is resection still the treatment of choice?,” *Hepatology*, vol. 47, no. 1, pp. 82–89, Jan. 2008, doi: 10.1002/HEP.21933.
- [38] F. J. Wolf, D. J. Grand, J. T. Machan, T. A. DiPetrillo, W. W. Mayo-Smith, and D. E. Dupuy, “Microwave Ablation of Lung Malignancies: Effectiveness, CT Findings, and Safety in 50 Patients,” *Radiology*, vol. 247, no. 3, pp. 871–879, Jun. 2008, doi: 10.1148/RADIOL.2473070996.
- [39] C. L. Brace, T. A. Diaz, J. L. Hinshaw, and F. T. Lee, “Tissue Contraction Caused by Radiofrequency and Microwave Ablation: A Laboratory Study in Liver and Lung,” *Journal of Vascular and Interventional Radiology*, vol. 21, no. 8, pp. 1280–1286, Aug. 2010, doi: 10.1016/J.JVIR.2010.02.038.

- [40] L. M. Veenendaal, A. De Jager, G. Stapper, I. H. M. Borel Rinkes, and R. Van Hillegersberg, "Multiple Fiber Laser-Induced Thermo-therapy for Ablation of Large Intrahepatic Tumors," *https://home.liebertpub.com/pho*, vol. 24, no. 1, pp. 3–9, Feb. 2006, doi: 10.1089/PHO.2006.24.3.
- [41] M. G. Skinner, M. N. Iizuka, M. C. Kolios, and M. D. Sherar, "A theoretical comparison of energy sources - microwave, ultrasound and laser - for interstitial thermal therapy," *Phys Med Biol*, vol. 43, no. 12, p. 3535, Dec. 1998, doi: 10.1088/0031-9155/43/12/011.
- [42] Y. Kim, H. Rhim, M. J. Choi, H. K. Lim, and D. Choi, "High-intensity focused ultrasound therapy: an overview for radiologists," *Korean J Radiol*, vol. 9, no. 4, pp. 291–302, 2008.
- [43] J. Van Der Zee, J. N. Peer-Valstar, P. J. M. Rietveld, L. De Graaf-Strukowska, and G. C. Van Rhoon, "Practical Limitations of Interstitial Thermometry During Deep Hyperthermia," *International Journal of Radiation Oncology\*Biophysics*, vol. 40, no. 5, pp. 1205–1212, Mar. 1998, doi: 10.1016/S0360-3016(98)00008-X.
- [44] R. Stollberger, P. W. Ascher, D. Huber, W. Renhart, H. Radner, and F. Ebner, "Temperature monitoring of interstitial thermal tissue coagulation using MR phase images," *Journal of Magnetic Resonance Imaging*, vol. 8, no. 1, pp. 188–196, Jan. 1998, doi: 10.1002/JMRI.1880080132.
- [45] A. Kickhefel *et al.*, "Clinical evaluation of MR temperature monitoring of laser-induced thermo-therapy in human liver using the proton-resonance-frequency method and predictive models of cell death," *Journal of Magnetic Resonance Imaging*, vol. 33, no. 3, pp. 704–709, 2011.
- [46] P. E. Huber *et al.*, "A new noninvasive approach in breast cancer therapy using magnetic resonance imaging-guided focused ultrasound surgery," *Cancer Res*, vol. 61, no. 23, pp. 8441–8447, 2001.

- [47] Phillips, “Investigational Sonalleve MR-HIFU fibroid therapy system showcased at ISMRM.” 2010. [Online]. Available: [http://incenter.medical.philips.com/doclib/enc/fetch/2000/4504/577242/577256/588821/5050628/5314862/6413113/FS40\\_Sonalleve\\_HIFU.pdf%3fnodeid%3d6412753%26vernunm%3d1](http://incenter.medical.philips.com/doclib/enc/fetch/2000/4504/577242/577256/588821/5050628/5314862/6413113/FS40_Sonalleve_HIFU.pdf%3fnodeid%3d6412753%26vernunm%3d1)
- [48] E. Minalga *et al.*, “An 11-channel radio frequency phased array coil for magnetic resonance guided high-intensity focused ultrasound of the breast,” *Magn Reson Med*, vol. 69, no. 1, pp. 295–302, Jan. 2013, doi: 10.1002/MRM.24247.
- [49] H. Odéen and D. L. Parker, “Magnetic resonance thermometry and its biological applications – Physical principles and practical considerations,” *Prog Nucl Magn Reson Spectrosc*, vol. 110, pp. 34–61, Feb. 2019, doi: 10.1016/J.PNMRS.2019.01.003.
- [50] W. Wlodarczyk *et al.*, “Comparison of four magnetic resonance methods for mapping small temperature changes,” *Phys Med Biol*, vol. 44, no. 2, p. 607, Feb. 1999, doi: 10.1088/0031-9155/44/2/022.
- [51] N. McDannold, “Quantitative MRI-based temperature mapping based on the proton resonant frequency shift: Review of validation studies,” *International Journal of Hyperthermia*, vol. 21, no. 6, pp. 533–546, 2009, doi: 10.1080/02656730500096073.
- [52] J. Yuan, C.-S. Mei, L. P. Panych, N. J. McDannold, and B. Madore, “Towards fast and accurate temperature mapping with proton resonance frequency-based MR thermometry,” *Quant Imaging Med Surg*, vol. 2, no. 1, pp. 21–32, 2012, doi: 10.3978/j.issn.2223-4292.2012.01.06.
- [53] A. Kickhefel, J. Roland, C. Weiss, and F. Schick, “Accuracy of real-time MR temperature mapping in the brain: A comparison of fast sequences,” *Physica Medica*, vol. 26, no. 4, pp. 192–201, Oct. 2010, doi: 10.1016/J.EJMP.2009.11.006.



- [54] G. Liu *et al.*, “Non-invasive temperature mapping using temperature-responsive water saturation shift referencing (T-WASSR) MRI,” *NMR Biomed*, vol. 27, no. 3, pp. 320–331, Mar. 2014, doi: 10.1002/NBM.3066.
- [55] C. J. Lewa and Z. Majewska, “Temperature relationships of proton spin-lattice relaxation time T1 in biological tissues.,” *Bull Cancer*, vol. 67, no. 5, pp. 525–530, Jan. 1980, Accessed: Jul. 17, 2023. [Online]. Available: <https://europepmc.org/article/med/6260272>
- [56] P. Baron, R. Deckers, F. M. Knuttel, and L. W. Bartels, “T1 and T2 temperature dependence of female human breast adipose tissue at 1.5 T: groundwork for monitoring thermal therapies in the breast,” *NMR Biomed*, vol. 28, no. 11, pp. 1463–1470, Nov. 2015, doi: 10.1002/NBM.3410.
- [57] V. Rieke and K. B. Pauly, “MR thermometry,” *Journal of Magnetic Resonance Imaging*, vol. 27, no. 2, pp. 376–390, Feb. 2008, doi: 10.1002/JMRI.21265.
- [58] P. Baron *et al.*, “In vivo T2-based MR thermometry in adipose tissue layers for high-intensity focused ultrasound near-field monitoring,” *Magn Reson Med*, vol. 72, no. 4, pp. 1057–1064, Oct. 2014, doi: 10.1002/MRM.25025.
- [59] N. Todd, M. Diakite, A. Payne, and D. L. Parker, “Hybrid proton resonance frequency/T1 technique for simultaneous temperature monitoring in adipose and aqueous tissues,” *Magn Reson Med*, vol. 69, no. 1, pp. 62–70, Jan. 2013, doi: 10.1002/MRM.24228.
- [60] M. A. Bernstein, K. F. King, and X. J. Zhou, *Handbook of MRI pulse sequences*. Elsevier, 2004.
- [61] J. Chen, B. L. Daniel, and K. B. Pauly, “Investigation of proton density for measuring tissue temperature,” *Journal of Magnetic Resonance Imaging*, vol. 23, no. 3, pp. 430–434, Mar. 2006, doi: 10.1002/JMRI.20516.

## Chapter 2

### 2 Hydroxyethylcellulose as a Tissue Mimicking Thermal Phantom Gel

To properly establish and test a method for measuring temperatures using MRI, a tissue-mimicking gel with appropriate temperature calibration is required. Thus, this chapter begins this process by testing the use of hydroxyethyl cellulose (HEC) gel doped with either copper (II) sulfate or gadobutrol as a potential thermal phantom material. With appropriate temperature properties, this gel would provide the benefits of having both tissue-mimicking permittivity and conductivity, as well as the ability to implement common thermometry sequences.

This chapter consists of a manuscript expanded from the peer-reviewed conference abstract, which has been submitted to *Physics in Medicine and Biology*:

Diego F. Martinez, Curtis N. Wiens, Chad T. Harris, William B. Handler, Blaine A. Chronik. *Hydroxyethylcellulose as a tissue mimicking phantom gel: Characterizing the temperature response at 0.5T*. International Society for Magnetic Resonance Imaging Annual Meeting 2023.

#### 2.1 Introduction

Surgical monitoring using magnetic resonance imaging (MRI) has increased dramatically over the past 15 years [1,2] stemming in large part from the development of minimally invasive thermal therapies. For example, in controlled hyperthermia, tissue is heated to  $\sim 45^{\circ}\text{C}$  for tens of minutes [3–6]. Likewise, in local thermal ablation, tissue is rapidly heated to  $>50^{\circ}\text{C}$  for seconds at a time [6,7]. Advancements in temperature precision, accuracy, and update rate from MR-based thermometry have enabled real-time temperature regulation [8–10].

Modern, specialized, mid-field (0.5 T) systems offer smaller size, lighter weight, and compact fringe field enabling easier siting and installation in locations apart from

diagnostic imaging, such as within (or adjacent to) the operating room [11–15]. Furthermore, these specialized mid-field systems offer an increased safety profile in comparison to high field for patients with implanted devices [16]. These properties are enticing for interventional monitoring albeit coming with a cost of reduced sensitivity to temperature-induced proton-resonance shifts [15,17].

MRI phantoms are a key component of development and validation of MRI systems, with several benefits over other validation methods. These phantoms can be designed to mimic tissue relaxation parameters, thermal conductivity, and shape. Mimicking many tissue parameters is important for a phantom, as it provides opportunity for further development of imaging methods and a simple way to validate the effectiveness of novel imaging techniques. Typically, phantoms use a solid or gel-like material as a base to match the viscosity of tissue, with agar [18,19], agarose [20], carrageenan gel [21], gelatin, polyvinyl alcohol [22,23], and polyacrylamide among common bases from which these phantoms are developed. In the case of agarose, a paramagnetic doping agent is used to reduce the  $T_1$  relaxation time, while the concentration of agarose modulates the  $T_2$  parameter. In other cases, the  $T_1$  and  $T_2$  parameters are both affected by gel concentration, such as in the use of carrageenan gel [21]. The drawback to phantom methods is changes in physical parameters (e.g., viscosity and conductivity) as the concentration of gelling agent changes or the phantom heats, which can lead to inconsistencies in behaviour when testing novel methods for thermometry.

Among gel candidates, hydroxyethyl cellulose (HEC) has many possible benefits as a tissue-mimicking phantom. Commonly used as part of the ISO/TS 10974:2018 [24] standard for testing of heating of active implantable medical devices, HEC provides various conductivity and permittivity-modulated tissue formations based on different concentrations that allow for matching of high permittivity lossy tissues such as muscle, as well as thinner tissue such as blood [24]. Alongside the matching of these tissue properties, the standard formulation of the gel is well established and easy to follow.

The primary HEC use case is in safety testing of implantable medical devices. The higher viscosity of the HEC allows for slower heat convection, allowing HEC to be used to evaluate the measurement of temperature with high resolution and measure the ability to delineate heated regions within the phantom. These properties lend themselves well to use as a thermometry phantom for development of thermal-mapping methods. As was mentioned earlier, thermal therapies can have wide temperature ranges and clinical requirements – a good measure of a phantom would be one that can be used for testing within several of these application therapy ranges. Given the long  $T_1$  values of undoped HEC, doping agents are typically required to reach target baseline  $T_1$  times matching target tissue.

The purpose of this work was to validate the viability of HEC gel for use as a thermal phantom. To validate the viability of HEC gel, the  $T_1$  relaxation time, PRF, and ADC of HEC gel were measured at different temperatures. These measurements resulted in temperature calibration curves for each parameter.

## 2.2 Materials and Methods

### 2.2.1 Phantom Production

Batches of HEC (Sigma-Aldrich; St. Louis, MO) gel were produced at 2% and 3% concentrations to create a phantom in accordance with the method outlined in Annex L [24] of the ISO/TS 10974:2018 standard. Specific chemical formulations for the 2% and 3% concentrations were: 2% HEC, 97.71% water, 0.294% NaCl (Sigma-Aldrich; St. Louis, MO); and 3% HEC, 96.85% water, 0.15% NaCl) respectively.

To reduce the  $T_1$  relaxation time of the gel and match this to known values of  $T_1$  in human brain grey matter, MR doping agents copper (II) sulfate ( $\text{CuSO}_4$ ; Sigma-Aldrich; St. Louis, MO) and gadobutrol (Gadovist; Bayer AG; Leverkusen, Germany) were added to make two sets of gels with varying concentrations of each.  $\text{CuSO}_4$  concentrations ranged between 0.5 mM and 3.0 mM, while the Gadobutrol concentrations ranged

between 0.075 mM and 0.2 mM. These solutions were placed in 50 ml falcon tubes for property characterization, with set up shown in **Figure 2.1**.

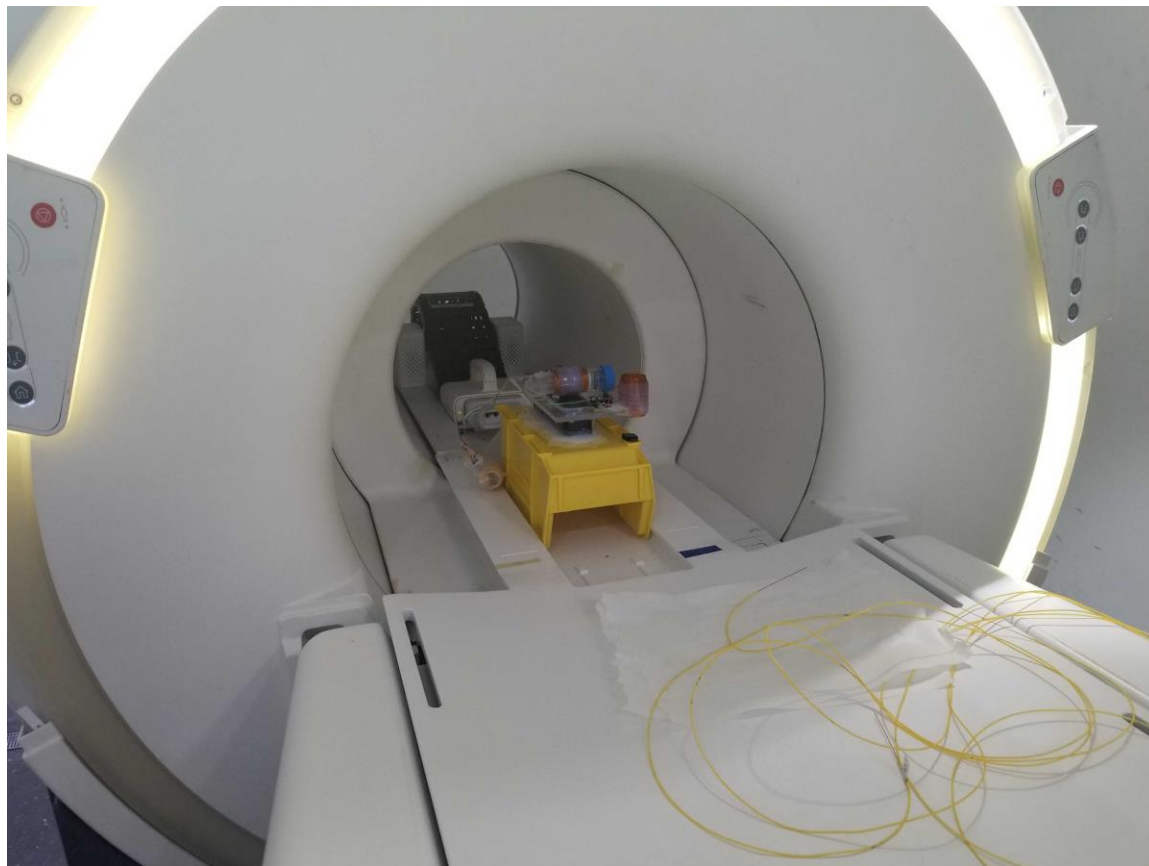


**Figure 2.1:** Experimental set up, with falcon tubes holding candidate solutions shown, along with the two solenoid coils used for testing and reference.

### 2.2.2 $T_1$ and $T_2$ Characterization

All relaxation time measurements were performed on a 0.5T head-only MR scanner (Synaptive Medical; Toronto, Canada) equipped with either an 8-channel head coil ( $T_2$  measurements) or a custom small diameter 2-channel coil, each a solenoid ( $T_1$  measurements).

The  $T_1$  relaxation time of each solution was individually measured using an inversion recovery free induction decay (FID) sequence. Acquisition parameters were 20 log-spaced inversion times between 10-3000 ms, 256 readout points, BW = 50 kHz, flip

angle = 180° then 90°, TR = 3.25 s. For each measurement the inversion recovery curve was fit to give estimate values for  $T_1$  using the relation

$$M = M_0(1 - 2e^{-TI/T_1} + e^{-TR/T_1}) \quad (2.1)$$

The  $T_2$  relaxation time of each solution was simultaneously measured using a set of spin echo images with different echo times. Acquisition parameters were: 2x2mm in-plane resolution, BW = 24 kHz, flip angle = 34°, 2 ms RF pulse duration, TR = 205 ms, with echo times between 10-150 ms. Mean and standard deviation values from manually drawn ROIs on the set of ten collected echo time images were found and fit to a  $T_2$  decay curve using

$$M = M_0 e^{-TE/T_2} \quad (2.2)$$

### 2.2.3 Temperature Calibration Curves

Candidate  $\text{CuSO}_4$  and Gadobutrol solutions were selected for  $T_1$  that best mimicked brain tissue at 0.5 T [25].  $T_1$ , PRF, and ADC temperature calibration curves were measured for these solutions on the same MR system using the custom small diameter 2 channel solenoid coil.

Temperature calibration curves were measured for each candidate solution by heating the solution using a monitored water bath. Repeated acquisitions were acquired while the solution cooled back to room temperature. To ensure a homogenous temperature in the region of interest, a 3-minute delay was added between removal from the bath and when acquisitions began using a stopwatch. This delay time was determined by benchtop testing with similar experimental setup. While cooling, the temperature was monitored using a calibrated fibre optic temperature probe connected to a tracking system ( $\pm 1^\circ\text{C}$ , 0.1°C resolution, -20 to 80°C range) (NOMAD-touch; Qualitrol; Fairport, NY). To account for the change in temperature over long acquisition intervals, the average

temperature over each acquisition was used as the measurement. The difference in temperature between the start and end times of each acquisition interval was used to estimate a temperature uncertainty.

#### 2.2.4 $T_1$ Temperature Calibration

To calibrate the  $T_1$  parameter with temperature,  $T_1$  cooling curves were measured in three successive steps with initial temperatures of 34°C, 41°C, and 51°C. For each set of measurements, the solutions were allowed to cool to room temperature while multiple inversion recovery FIDs (see previous  $T_1$  measurement description) were acquired repeatedly.

#### 2.2.5 PRF Temperature Calibration

PRF temperature calibration was performed for each candidate solution using an FID sequence. Acquisition parameters were TR = 6000 ms; readout points = 256; BW = 25 kHz; flip angle = 90°. To remove the confounding factor of B0 field drift, the second solenoid coil simultaneously measured the frequency of room temperature water doped with CuSO<sub>4</sub> ( $T_1$  ~629 ms). The PRF response was therefore measured as the difference in frequency between the cooling candidate solution and the room temperature reference, with a total acquisition time of 30 minutes.

#### 2.2.6 ADC Temperature Calibration

ADC was measured with an EPI based diffusion weighted imaging sequence (10 slices, matrix size = 100x50, 1.6x1.6x2 mm<sup>3</sup> resolution, TE = 74.7 ms, TR = 4000 ms, flip angle = 90°, b = 750). ADC values for each time point were averaged over a central 25x6.25x8mm region of the slice stack.

### 2.3 Results

$T_1$  and  $T_2$  values for all concentrations are shown in **Figure 2.2a-d**. Candidate solutions of 3% HEC doped with 2mM CuSO<sub>4</sub> and 0.2mM Gadobutrol produced  $T_1$ s of 659 ms and 705 ms and  $T_2$ s of 127 ms and 129 ms at room temperature respectively. The  $T_1$  and  $T_2$

values of the doped gel matched the  $T_1$  and  $T_2$  of GM in the brain at 0.55 T closely ( $T_1 \sim 712$  ms [11,25] and  $T_2 \sim 112$  ms [25]), matching within 8% and 15% respectively.

The  $T_1$  relaxivity parameter for the  $\text{CuSO}_4$  and Gadobutrol candidate solutions of HEC as temperature varies is shown in **Figure 2.3**. The rate of change of  $T_1$  relaxation with respect to temperature was found to be  $(17.1 \pm 0.07)$  ms/ $^\circ\text{C}$  for the Copper (II) Sulfate formulation and  $(16.9 \pm 0.13)$  ms/ $^\circ\text{C}$  for the Gadobutrol formulation. Several runs were repeated at increasing temperatures to evaluate any possible sample breakdown due to ionization of  $\text{CuSO}_4$  or de-chelation of the Gadobutrol agent. The repeated runs at higher temperatures did not produce a noticeable drift in the  $T_1$  parameter, as the lower temperatures produced consistent  $T_1$  values.

Measurement of the change in resonance frequency as temperature varies is shown in **Figure 2.4**. The  $\alpha$  temperature parameter of the  $\text{CuSO}_4$  and Gadobutrol solutions were found to be  $(-8.74 \pm 0.12) \times 10^{-3}$  ppm/ $^\circ\text{C}$  and  $(-8.42 \pm 0.08) \times 10^{-3}$  ppm/ $^\circ\text{C}$  respectively.

Measurement of the ADC parameter as temperature varies is shown in **Figure 2.5**. Linear fit resulted in an ADC vs temperature slope of  $(5.34 \pm 0.063) \times 10^{-5}$  mm<sup>2</sup>/s/ $^\circ\text{C}$  for the Copper (II) Sulfate formulation and a slope of  $(4.26 \pm 0.059) \times 10^{-5}$  mm<sup>2</sup>/s/ $^\circ\text{C}$  for the gadobutrol formulation.



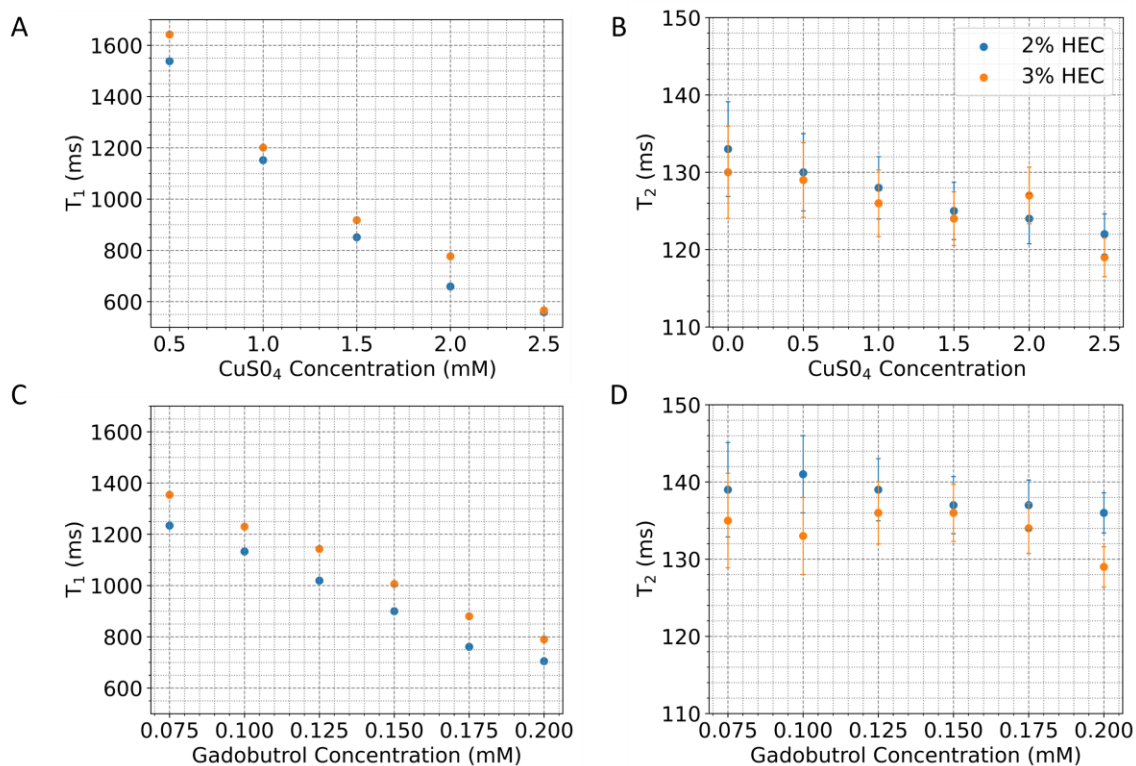


**Figure 2.2:**  $T_1$  and  $T_2$  relaxation times for sample mixtures of Hydroxyethyl Cellulose Concentrations of 2% (blue) and 3% (orange). **A-B** shows  $T_1$  and  $T_2$  with samples doped using  $\text{CuSO}_4$  with concentrations between 0-2.5 mM. **C-D** show  $T_1$  and  $T_2$  for samples doped with Gadobutrol with concentrations between 0.075-0.200 mM. The trends show a decrease in  $T_1$  time as both doping agent concentrations are increased, while  $T_2$  times are not significantly affected by the change in either doping concentrations or HEC formulation. Uncertainties in figures **A** and **C** are  $\sim 10$  ms and cannot be seen on this scale.

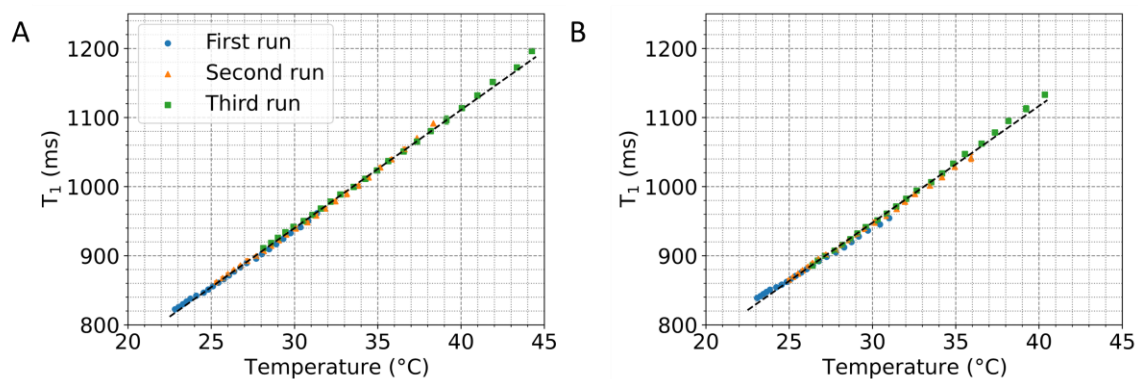


**Figure 2.3:** T<sub>1</sub> relaxation time for a 3% HEC formulation

(A) CuSO<sub>4</sub> doped to 2.0 mM and (B) Gadobutrol doped to a 0.2mM concentration. Several runs were repeated at increasing temperatures to evaluate any possible sample decay due to ionization of CuSO<sub>4</sub> or chelation of the Gadobutrol agent. T<sub>1</sub> at these temperatures remained consistent when compared to other runs at the same temperature point.  $R^2 = 0.998$  for (A) and  $R^2 = 0.9945$  for (B). The rate of change of T<sub>1</sub> relaxation are  $(17.1 \pm 0.07)$  ms/°C for the Copper (II) Sulfate formulation and  $(16.9 \pm 0.13)$  ms/°C for the Gadobutrol formulation. Uncertainties in both figures may be hard to see, and are ~10 ms.

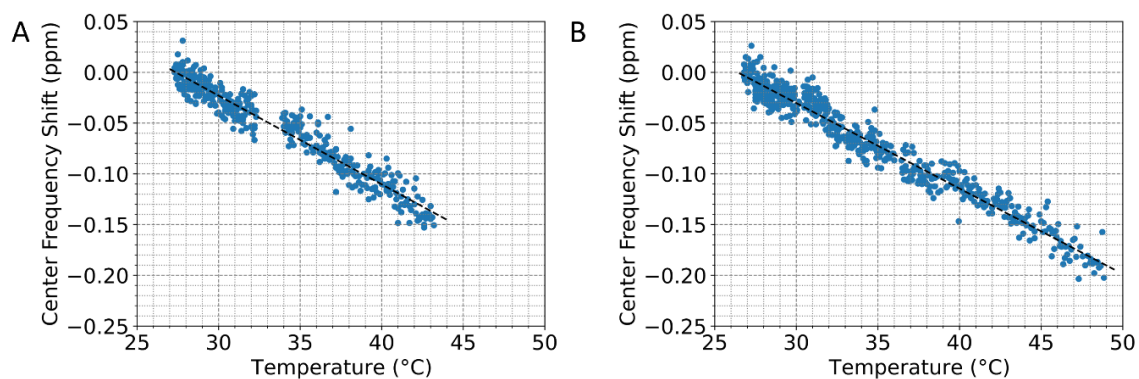


**Figure 2.4:** Change in Central Frequency vs Temperature

(**A**) a 2.0 mM CuSO<sub>4</sub> doped sample of 3% HEC gel and (**B**) a 0.200 mM sample doped with Gadobutrol.  $R^2=0.9351$  for (**A**) and  $R^2=0.9536$  for (**B**). Alpha temperature parameter of  $(-8.74 \pm 0.12) \times 10^{-3}$  ppm/C was obtained using a linear fit for the CuSO<sub>4</sub> sample, and  $(-8.42 \pm 0.08) \times 10^{-3}$  ppm/C was obtained for the Gadobutrol sample.

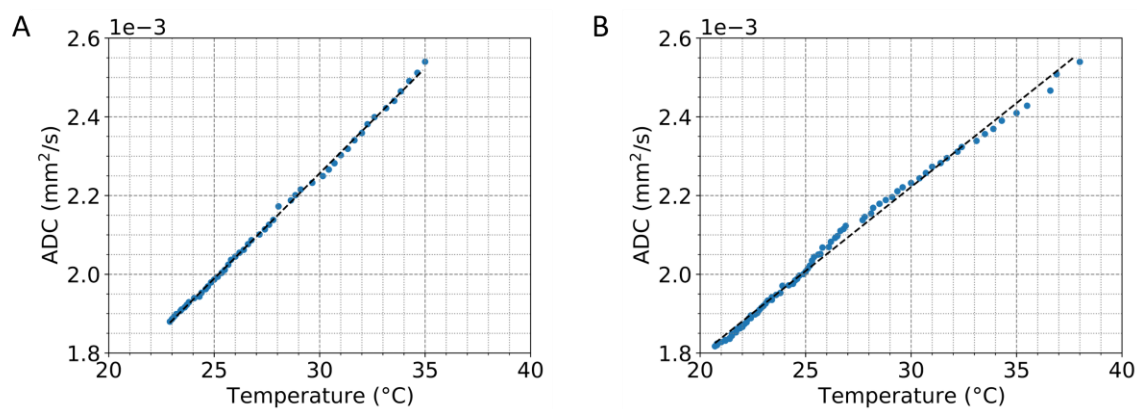


**Figure 2.5:** Change in Apparent Diffusion Coefficient vs temperature Measured on a 3% formulation of HEC with (A) sample of 2mM  $\text{CuSO}_4$  and (B) sample of 0.200 mM Gadobutrol.  $R^2 = 0.9889$  for (A) and  $R^2 = 0.9941$  for (B). Linear fit resulted in ADC vs temperature slope of  $(5.34 \pm 0.063) \times 10^{-5} \text{ mm}^2/\text{s}/^{\circ}\text{C}$  for the Copper (II) Sulfate formulation and a slope of  $(4.26 \pm 0.059) \times 10^{-5} \text{ mm}^2/\text{s}/^{\circ}\text{C}$  for the Gadobutrol formulation.

## 2.4 Discussion

In this work, parameter temperature calibrations for common concentrations of HEC gel doped with two different agents were conducted over the range 25 to 50 degrees. This temperature range is common for hyperthermia treatment with applications in drug delivery and cancer therapy [6]. An additional use case is in Neonatal body cooling, where target cooling temperatures reach 33°C [26]. This therapy involves a prolonged cooling with large cooling pads and provides a great use case for thermal tracking using MRI. Typical treatment lengths in these therapies last hours to days, which suits the nature of temperature tracking in the hour range using MRI, along with the potential for follow up scans to measure temperature throughout the body as treatment progresses, including helping safely conduct the warming phase once the cooling therapy has concluded.

The doping agents used in this work did not substantially affect the  $T_2$  relaxation parameter of the gel. This was to our advantage as the  $T_2$  remained relatively close to that of brain tissue at 0.5 T over all concentrations tested. For a more accurate measure of  $T_2$ , a CPMG approach could be used, as this could suppress distortions.

If there were a need for the  $T_2$  value to be modulated, Manganese Chloride (MnCl) could be a suitable additional doping agent as it is a well established  $T_2$  modifier, and previous work has successfully combined MnCl with CuSO<sub>4</sub> to achieve a combination of  $T_1/T_2$  target values [21].

The  $T_1$  temperature dependence fell well within the expected shift of 2-3%/°C reported across field strengths [2]. In the  $T_1$  temperature scans, the response curve was roughly linear in the tested range. Furthermore, each run at progressively higher initial temperatures was found to be consistent, with the  $T_1$  at the same temperatures matching as the sample cooled. This reproducibility suggests that the gel itself is unaffected by heating cycles up to 51°C temperature. Previous work on  $T_1$  based temperature mapping have noted that tissue exhibits a non-linear  $T_1$  temperature response beyond ~45°C [3,4].

Although this study did not examine extreme heating cases beyond this general range, there is the possibility that heating beyond the tested region could show a similar non-linear  $T_1$  behaviour.

Both gel formulations had similar PRF alpha coefficients and ADC coefficients within the range of reported values between  $-0.0111$  and  $-0.00674$  ppm/ $^{\circ}\text{C}$  (dependent on tissue type)<sup>3</sup> and  $2.0$ - $2.5\%$ / $^{\circ}\text{C}$  [24] respectively. This suggests the choice of doping agent is flexible and can be guided by availability or cost. When testing ADC using the gadobutrol doped HEC however, a deviation was observed while cooling, which would suggest  $\text{CuSO}_4$  may be more suitable.

The temperature calibration of HEC gels was measured at  $0.5$  T. Despite only measuring at one field strength, HEC gels should be a suitable candidate for thermal phantoms at any field strength. To use at HEC gels at a different field strength, optimization of  $\text{CuSO}_4$  or gadobutrol concentrations for target  $T_1$  and  $T_2$  relaxation times would need to be performed. Secondly,  $T_1$  temperature calibration would also be expected to change with field strength. In contrast, the theoretical expectation is that the central frequency and ADC parameters would be unchanged across field strengths.

## 2.5 Conclusion

This work provides the method for creating phantom gels with properties favorable to the testing of  $T_1$ , PRF, and ADC thermal mapping techniques. By using HEC, a known tissue mimicking gel, and a doping agent of either Copper (II) Sulfate or Gadobutrol, the relaxation parameters can be set to match typical human brain tissue parameters. The gels produced offer consistent, replicable  $T_1$  and PRF temperature parameters which are valid in the range of  $33$ - $50^{\circ}\text{C}$ , as well as a linear temperature response to the apparent diffusion coefficient derived via diffusion weighted imaging.

## 2.6 References

- [1] Rieke, V. & Pauly, K. B. MR thermometry. *Journal of Magnetic Resonance Imaging* 27, 376–390 (2008).
- [2] Odéen, H. & Parker, D. L. Magnetic resonance thermometry and its biological applications – Physical principles and practical considerations. *Prog Nucl Magn Reson Spectrosc* 110, 34–61 (2019).
- [3] Diakite, M., Payne, A., Todd, N. & Parker, D. L. Irreversible change in the T1 temperature dependence with thermal dose using the proton resonance frequency-T1 technique. *Magn Reson Med* 69, 1122–1130 (2013).
- [4] Peller, M. et al. T1 relaxation time at 0.2 Tesla for monitoring regional hyperthermia: feasibility study in muscle and adipose tissue. *Magnetic Resonance in Medicine: An Official Journal of the International Society for Magnetic Resonance in Medicine* 47, 1194–1201 (2002).
- [5] Fiorito, M., Yushchenko, M., Cicolari, D., Sarracanie, M. & Salameh, N. Fast, interleaved, Look-Locker-based T1 mapping with a variable averaging approach: Towards temperature mapping at low magnetic field. *NMR Biomed* 36, e4826 (2023).
- [6] Blackwell, J. et al. Proton Resonance Frequency Shift Thermometry: A Review of Modern Clinical Practices. *Journal of Magnetic Resonance Imaging* 55, 389–403 (2022).
- [7] Van Rhoon, G. C. & Wust, P. Introduction: Non-invasive thermometry for thermotherapy. *International Journal of Hyperthermia* 21, 489–495 (2005).
- [8] Svedin, B. T., Payne, A. & Parker, D. L. Simultaneous proton resonance frequency shift thermometry and T1 measurements using a single reference variable flip angle T1 method. *Magn Reson Med* 81, 3138–3152 (2019).

- [9] Zhang, L., Armstrong, T., Li, X. & Wu, H. H. A variable flip angle golden-angle-ordered 3D stack-of-radial MRI technique for simultaneous proton resonant frequency shift and T1-based thermometry. *Magn Reson Med* 82, 2062–2076 (2019).
- [10] Kellman, P. et al. Optimized saturation recovery protocols for T1-mapping in the heart: influence of sampling strategies on precision. *Journal of Cardiovascular Magnetic Resonance* 16, 1–15 (2014).
- [11] Campbell-Washburn, A. E. et al. Opportunities in interventional and diagnostic imaging by using high-performance low-field-strength MRI. *Radiology* 293, 384–393 (2019).
- [12] Odéen, H., Hofstetter, L., Kim, S.-E. & Parker, D. L. High spatial and temporal resolution absolute temperature imaging of Ethylene Glycol. *Proc 30th Annu Meet ISMRM London UK* (2022).
- [13] Lewin, J. S., Metzger, A. & Selman, W. R. Intraoperative Magnetic Resonance Image Guidance in Neurosurgery. *Journal of Magnetic Resonance Imaging* 12, 512–524 (2000).
- [14] Coffey, A. M., Truong, M. L. & Chekmenev, E. Y. Low-field MRI can be more sensitive than high-field MRI. *Journal of Magnetic Resonance* 237, 169–174 (2013).
- [15] Marques, J. P., Simonis, F. F. J. & Webb, A. G. Low-field MRI: An MR physics perspective. *Journal of Magnetic Resonance Imaging* 49, 1528–1542 (2019).
- [16] Connell, I. R., Panther, A. & Chronik, B. A. Specific Absorption Rate in Head-Only Mid-Field Scanner: Comparisons to 1.5 T and 3 T. in *Proc Intl Soc Mag Reson Med* vol. 27 4167 (2019).
- [17] Webb, A. & O'Reilly, T. Tackling SNR at low-field: a review of hardware approaches for point-of-care systems. *Magnetic Resonance Materials in Physics, Biology and Medicine* 1–19 (2023) doi:10.1007/S10334-023-01100-3/FIGURES/8.



- [18] Bucciolini, M., Ciraolo, L. & Lehmann, B. Simulation of biologic tissues by using agar gels at magnetic resonance imaging. *Acta radiol* 30, 667–669 (1989).
- [19] Vre, R. M., Grimee, R., Parmentier, F. & Binet, J. The use of agar gel as a basic reference material for calibrating relaxation times and imaging parameters. *Magn Reson Med* 2, 176–179 (1985).
- [20] Howe, F. A. Relaxation times in paramagnetically doped agarose gels as a function of temperature and ion concentration. *Magn Reson Imaging* 6, 263–270 (1988).
- [21] Yoshimura, K. et al. Development of a tissue-equivalent MRI phantom using carrageenan gel. *Magn Reson Med* 50, 1011–1017 (2003).
- [22] Surry, K. J. M., Austin, H. J. B., Fenster, A. & Peters, T. M. Poly(vinyl alcohol) cryogel phantoms for use in ultrasound and MR imaging. *Phys Med Biol* 49, 5529 (2004).
- [23] Mano, I., Goshima, H., Nambu, M. & Iio, M. New polyvinyl alcohol gel material for MRI phantoms. *Magn Reson Med* 3, 921–926 (1986).
- [24] International Organization for Standardization (ISO). Assessment of the safety of magnetic resonance imaging for patients with an active implantable medical device. (2018).
- [25] Campbell-Washburn, A., Herzka, D., Kellman, P., Koretsky, A. & Balaban, R. Image contrast at 0.55 T. *ISMRM 27th Scientific Sessions* 1214 (2019).
- [26] Tagin, M. A., Woolcott, C. G., Vincer, M. J., Whyte, R. K. & Stinson, D. A. Hypothermia for Neonatal Hypoxic Ischemic Encephalopathy: An Updated Systematic Review and Meta-analysis. *Arch Pediatr Adolesc Med* 166, 558–566 (2012).

## Chapter 3

### 3 Echo Planar Imaging Proton Resonant Frequency temperature mapping at 0.5T: Comparison to Single-Echo

Once a suitable formulation for a novel tissue-mimicking phantom gel has been established, the next challenge becomes implementing sequences that can measure temperature on a custom-built phantom made to measure temperature. This work implements temperature mapping using several methods and addresses the balancing act that is required to optimize imaging parameters while maintaining an acceptable update rate.

This chapter consists of a manuscript expanded from the peer-reviewed conference abstracts:

Diego F. Martinez, Chad T. Harris, Curtis N. Wiens, William B. Handler, Blaine A. Chronik. *Monitoring Temperature using Gradient Echo Imaging at 0.5T*. International Society for Magnetic Resonance Imaging Annual Meeting 2023.

Chad T. Harris, Curtis N. Wiens, Diego F. Martinez, Andrew T. Curtis, Blaine A. Chronik. *Optimization of EPI based PRF thermometry at 0.5 T*. International Society for Magnetic Resonance Imaging Annual Meeting 2023.

#### 3.1 Introduction

Thermal therapies are an established clinical treatment protocol for a variety of ailments and refer to the medical application of heating or cooling to the body for therapeutic purposes [1,2]. Heat therapy, also known as hyperthermia treatment, involves the use of various energy sources, such as radiofrequency, laser, microwave, or ultrasound, to generate controlled heat as a common treatment for treating a variety of tumors [3–6]. This

technique offers several advantages, including a reduced risk of complications, shorter recovery time, and potential for outpatient treatment, making it a valuable alternative to invasive traditional surgical interventions. On the mild range of hyperthermia treatments are applications where tissue is heated up to the range of  $\sim 50^{\circ}\text{C}$  for treatments of minutes to hours, while high temperature hyperthermia can reach temperatures far beyond this for shorter treatment times.

On the other hand, cold therapy, also called cryotherapy, utilizes cold temperatures through ice packs, cold compresses, or specialized chambers to constrict blood vessels, reduce inflammation, and numb nerve endings [7,8]. Especially promising is the use of body cooling in infants suffering from hypoxic-ischemic encephalopathy [9], where treatments can either involve cooling the head or the entire body to target temperatures of  $34.5^{\circ}\text{C}$  and  $33.5^{\circ}\text{C}$  respectively [7,8,10]. At the conclusion of the treatment, infants are re-warmed over the span of 6 to 12 hours, at a rate of  $0.5^{\circ}\text{C}/\text{hour}$ . The benefit of both treatment methods is the non-invasive nature, which can reduce patient contact and minimize complications.

MR imaging in the mid-field strengths (0.5 T) offers some possibilities for monitoring of interventional temperature treatment procedures [11]. The compact design and small fringe fields allow for lessened siting requirements, and operating at this lower field strength provides lower susceptibility-based geometric distortion, along with reduced tissue heating during operation [12–14]. However, there is a signal-to-noise (SNR) loss at this field strength, along with a slower precession of nuclei compared to higher field strengths [15]. In the context of providing interventional temperature tracking, imaging at this field strength provides a variety of potential benefits that could be leveraged [16]. The small fringe fields offer the potential for the MR system to be safely placed in a surgical suite, and the modern mid-field magnets have a quick ramp time which allows the magnet to be turned on or off within minutes. Specialized head-only systems with a reduced bore size are also easier to fit into non-specialized locations. The reduced tissue heating is

particularly relevant in populations with implantable medical devices, which can be precluded from receiving MR scans at higher field strength [17].

MR thermometry can be used to non-invasively track temperatures and has been shown to measure temperatures in ranges between 20°C to 100°C [1]. In measuring temperature, various tissue parameters have been explored as candidates, including  $T_1$  change, apparent diffusion coefficient change, magnetization transfer, and proton density imaging. However, most studies that track thermal therapies have used the proton resonant frequency shift (PRF) method [18–20], now the preferred method for thermometry. By measuring the shift in sequential MR phase acquisitions using a gradient echo acquisition, a temperature map can be determined based on this known relation between temperature and hydrogen bonding.

Performing temperature mapping on a mid-field system provides opportunities and challenges for implementation of a PRF approach. As the Larmor frequency is proportional to main field  $B_0$ , the slower accrual of phase at lower field suggests that longer echo times (TE) are required to generate equivalently large phase as high-field. Due to a longer  $T_2^*$  at mid-field strength, longer TEs can be used with less degradation from  $T_2^*$  dispersion. Taking advantage of this longer acceptable echo time can be challenging, as increasing the echo time to approach the  $T_2^*$  will cause a trade-off in either spatial coverage or resolution (to maintain an acceptable update rate), or in temporal resolution (requiring gaps between image updates).

While the current standard approach involves using a single echo gradient recalled echo (SE-GRE) acquisition, it might be beneficial to consider alternative approaches which can offer a better temporal resolution without affecting coverage or resolution. One way to bridge this gap involves using the particularly well-suited echo planar imaging (EPI)

sequence for temperature mapping [21,22], as lengthened  $T_2^*$  values in the mid-field can be leveraged in ways a SE-GRE sequence cannot without prohibitively slow update rates.

This study serves to firstly produce a high-quality temperature control phantom for comparisons of temperature mapping. Further, the capabilities of implementation of a SE-GRE based approach to thermal mapping and explore the possible benefits that can be achieved by implementation of an EPI based approach to thermal mapping. These comparisons were done both in vivo, evaluating the temperature uncertainty over an 8-minute scanning period, and in the phantom where a cooling experiment compared the abilities to track temperatures while monitored using a temperature probe.

## 3.2 Methods

Phantom temperature stability and in vivo temperature tracking experiments were performed using three acquisitions. Imaging parameters for each acquisition are shown in **Table 3.1**. The first acquisition was a SE-GRE with a 7.8 s update rate. The second acquisition was an EPI acquisition with spatial coverage, spatial resolution, and temporal resolution matching that of the single echo gradient echo reference acquisition. The third acquisition was an EPI acquisition with faster update rates and improved spatial coverage. All imaging was acquired on a head-specific 0.5 T MR system (Synaptive Medical, Toronto, Ontario) equipped with an 8-channel head coil.

### 3.2.1 Phantom Production

A custom double-nested cylinder was produced, with the outer layer acting as a reference region, and the inner cylinder resting in polyurethane foam susceptibility matched using Pyrolytic Graphite [23]. A schematic of the phantom is shown in **Figure 3.1**. The outer cylinder has a diameter of 12.7 cm, with an inner diameter of 8.9 cm and a length of 10.7 cm. The inner sample container was a 120 ml tube, with a length of 7 cm. Previous phantom design exploration shown in **Appendix A**.

The susceptibility matching foam was created by dispersing pyrolytic graphite at a volume fraction of 0.045 to match tissue susceptibility of  $-9$  ppm into one component of a two-component polyurethane foam [Smooth-On, Macungie, Pennsylvania, USA]. This foam was molded to the shape of the sample container. In both the sample and the outer cylinder, a probe insert was made to allow access for an optical temperature probe to be placed in either gel.

Hydroxyethylcellulose (HEC) was used as a tissue-mimicking gel inside of the phantom, produced using the method described in Annex L of the ISO 10974:2018 standard [24], for the solution with 96.85% water, 3% HEC [SigmaAldrich; St. Louis, Mo], and 0.15% NaCl, giving a relative dielectric permittivity of 78, conductivity of 0.47 S/m, density of 1001 kg/m. The HEC gel was then doped using copper (II) sulfate [Sigma-Aldrich; St. Louis, Mo] to a 2 mM concentration to produce a  $T_1$  relaxation time like brain tissue with a previously measured (see **Chapter 2**)  $T_1$  of 659 ms. Similarly, the alpha parameter required for PRF thermometry was calculated by simultaneously measuring the center frequency and the temperature as a sample of heated HEC gel cooled, with reported value of  $-0.00874$  ppm/ $^{\circ}\text{C}$ .

Anatomical 3D EPI images of the thermometry phantom were acquired. Imaging parameters were: Flip angle =  $83^{\circ}$ , TR = 1555 ms, TE = 70 ms, bandwidth = 160 kHz, matrix size =  $110 \times 90 \times 13$ , field of view =  $22 \times 18$  cm<sup>2</sup>, slice thickness = 3.0 mm, acquisition time = 2 m 36.5 s.

### 3.2.2 Temperature-Stability Measurement

*In vivo* temperature-stability images were provided by Synaptive Medical to the xMR labs. All imaging was acquired on a head-specific 0.5 T MR system (Synaptive Medical, Toronto, Ontario) equipped with an 8-channel head coil. For stability quantification a 3 slice SE-GRE, 3 slice EPI, a 13 slice EPI was taken over 64 time points. Imaging parameters for all acquisitions are shown in **Table 3.1**.

Parameter	Single Echo GRE	3-Slice EPI	13-Slice EPI
TE (ms)	23.75	70	70
TR (ms)	86	346.4	1508
$N_{\text{avg}}$	1	22	1
Update Rate (s)	7.8	7.602	1.508
RBW (kHz)	20	90	90
FOV (mm)	230x190	230x190	230x190
Slices	3	3	13
Slice Thickness (mm)	3.0	3.0	3.0
Matrix Size	110x90	110x90	110x90
Flip Angle ( $^{\circ}$ )	28	54	85

**Table 3.1:** Parameters for the three sequences used in the temperature stability and temperature tracking tests. 22 averages were taken on the 3-slice EPI acquisition to achieve a similar update rate to the SE-GRE sequence.

### 3.2.3 Temperature-Tracking Experiment

To validate the ability of tracking temperature change using the PRF method, the doped HEC gel in phantom described above was heated in a hot water bath to  $\sim 60^{\circ}\text{C}$ , then a fibre optic probe was inserted into the HEC gel acting as a thermometer, with tracking done on a NOMAD-Touch [Qualitrol; Fairport, NY] system ( $\pm 1^{\circ}\text{C}$ ;  $\pm 0.1^{\circ}\text{C}$  Resolution,  $-20$  to  $80^{\circ}\text{C}$  range, calibrated using a monitored hot water bath). The heated HEC sample was placed in the center of the phantom and a series of 256 repetitions (as opposed to the 64 repetitions taken for in vivo measurements) of the 3-slice SE-GRE and 3-slice EPI acquisitions described above were collected. Likewise, 1000 repetitions of the 13-Slice EPI were acquired.

### 3.2.4 Temperature-Map Reconstruction

The phase difference of each image was calculated with respect to the first time point. A first order polynomial fit of a reference region on the boundary of the brain was used to remove baseline phase changes [25]. Finally, voxel-wise standard deviations over the time series were computed on the phase and magnitude images to calculate temperature uncertainties and temporal SNR respectively.

### 3.3 Results

Firstly, a structural scan of the phantom used in the experiments is shown in **Figure 3.1B**, with the inner sample and outer reference regions seen. An in vivo comparison of temperature mapping method between the 3-slice SE-GRE and Echo Planar Imaging (EPI) described in **Table 3.1** are shown in **Figure 3.2A**. This figure shows voxel-wise temperature uncertainties in the three acquisitions taken to create a map showing the uncertainties in different regions. In particular, the mean temperature uncertainty over a set of 64 acquisitions in the phantom was found to be  $0.40^{\circ}\text{C}$  and  $0.33^{\circ}\text{C}$  in the SE-GRE and EPI respectively. Note that multiple tissues with different  $T_1$  and  $T_2$  parameters are used in this temperature stability measurement, with brain structure reflected in the temperature uncertainty maps. A 13-slice EPI acquisition is shown in **Figure 3.2B**, in a similar manner to the display of the 3-slice acquisitions. With a shorter update rate of 1.508 s, the average temperature uncertainty was  $1.15^{\circ}\text{C}$ , with a peak uncertainty of  $2.05^{\circ}\text{C}$ . As grey matter has a longer  $T_2$ , the white/grey matter structure can be clearly seen, with lower uncertainties in the grey matter due to a closer match to the 70 ms echo time used in the EPI sequence.

The experimental set up to test temperature tracking ability in the double-nested phantom is shown in **Figure 3.3**, where the use of the SEGRE approach is shown in **Figure 3.4**, with a temperature match and Bland-Altman plot showing the temperature uncertainty of  $1.28^{\circ}\text{C}$  while tracking cooling, along with sample slices during the cooling tracking. This is compared to the 22-average EPI approach found in **Figure 3.5**, where the Bland-Altman shows a tracking uncertainty range of  $0.85^{\circ}\text{C}$ . The images of the cooling experiment show some uneven cooling. Also, there is some tracking drift observed in the initial measurements as the cooling settled to a steady state in line with measurements made in the fibre optic thermometer. Testing of temperature tracking in a full coverage 13 slice EPI is shown in **Figure 3.6**. With a tracking uncertainty found from the Bland-Altman of  $1.0^{\circ}\text{C}$  and an update rate of 1.508s. The temperature tracking was seen to show some periodic temperature variation.



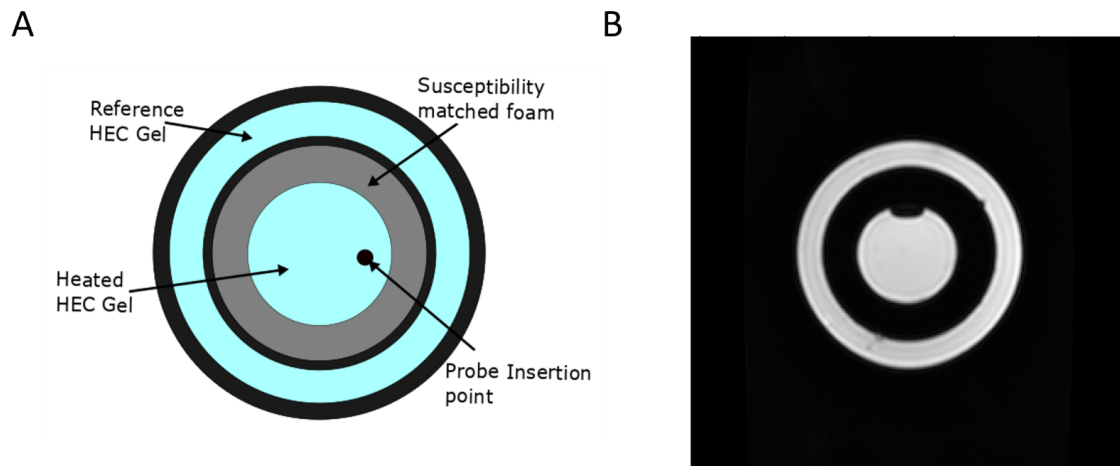


**Figure 3.1:** Schematic and MR scan of custom phantom

Schematic (A) and structural EPI scan (B) of the custom built phantom. The phantom is constructed of two concentric cylinders, with a susceptibility matched polyurethane foam used between to reduce susceptibility artifacts. The structural scan was done using a 13 slice EPI protocol with parameters Flip angle =  $83^\circ$ , TR = 1555 ms, TE = 70 ms, bandwidth = 160 kHz, matrix size = 110x90, field of view = 22x18 cm<sup>2</sup>, acquisition time = 2m 36.5s, Number of averages taken = 101.

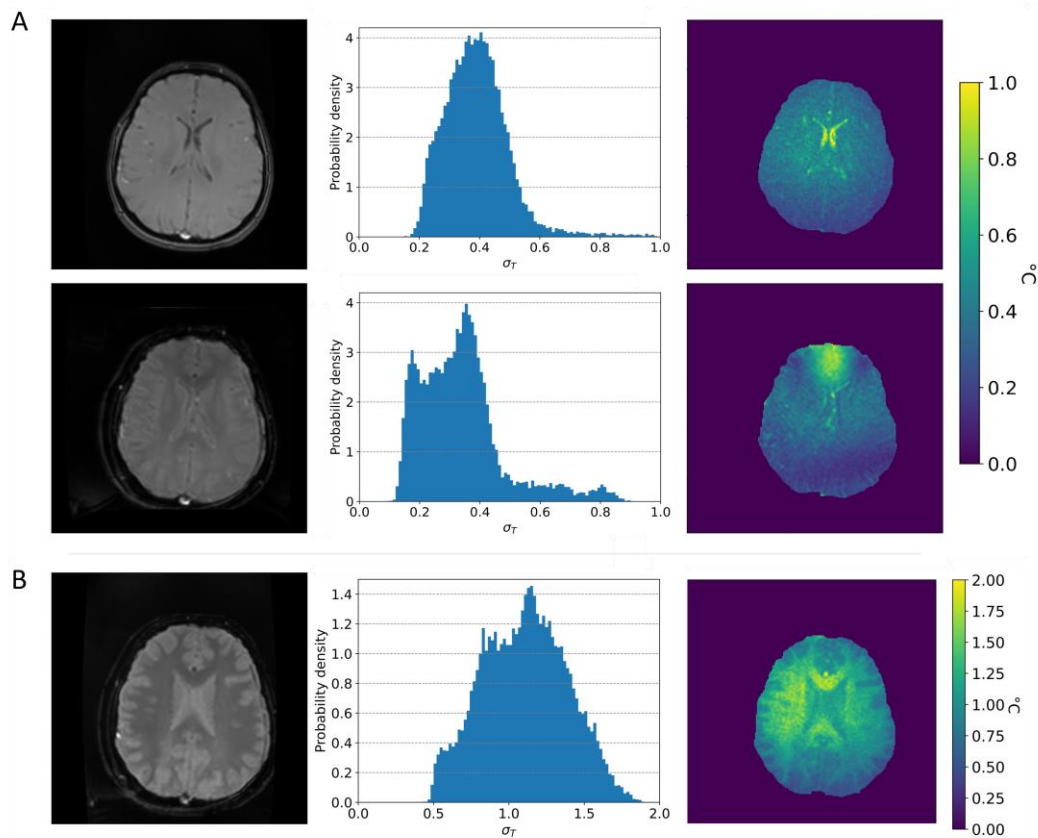


**Figure 3.2:** Comparison of SE-GRE and EPI in vivo

(A) Comparison of a single echo Gradient Recalled Echo temperature mapping (top row), vs an Echo Planar Imaging thermometry approach (second row). Both sequences measured over a set of 64 acquisitions, with parameters shown in **Table 3.1**. Structural scans shown on the left, with a histogram of temperature stability as a probability density function in the middle, and Temperature Stability map on the right. The Single Echo GRE average temperature uncertainty over the slice was  $0.40^{\circ}\text{C}$  with a peak uncertainty of  $1.0^{\circ}\text{C}$  in the brain stem. In the EPI case, temperature stability over the slice averaged  $0.33^{\circ}\text{C}$  with a peak uncertainty of  $0.90^{\circ}\text{C}$ . (B) Structural (left), and Temperature Stability (histogram in middle and map right) scan measured using 64 EPI acquisitions over a full coverage of 13 slices, with parameters shown in **Table 3.1**. With a 1.508 s update rate, temperature stability over the slice averaged  $1.15^{\circ}\text{C}$  with a peak uncertainty of  $2.05^{\circ}\text{C}$ . Structure can more clearly be seen in the temperature stability figure; more exact temperature mapping possible in the gray matter.

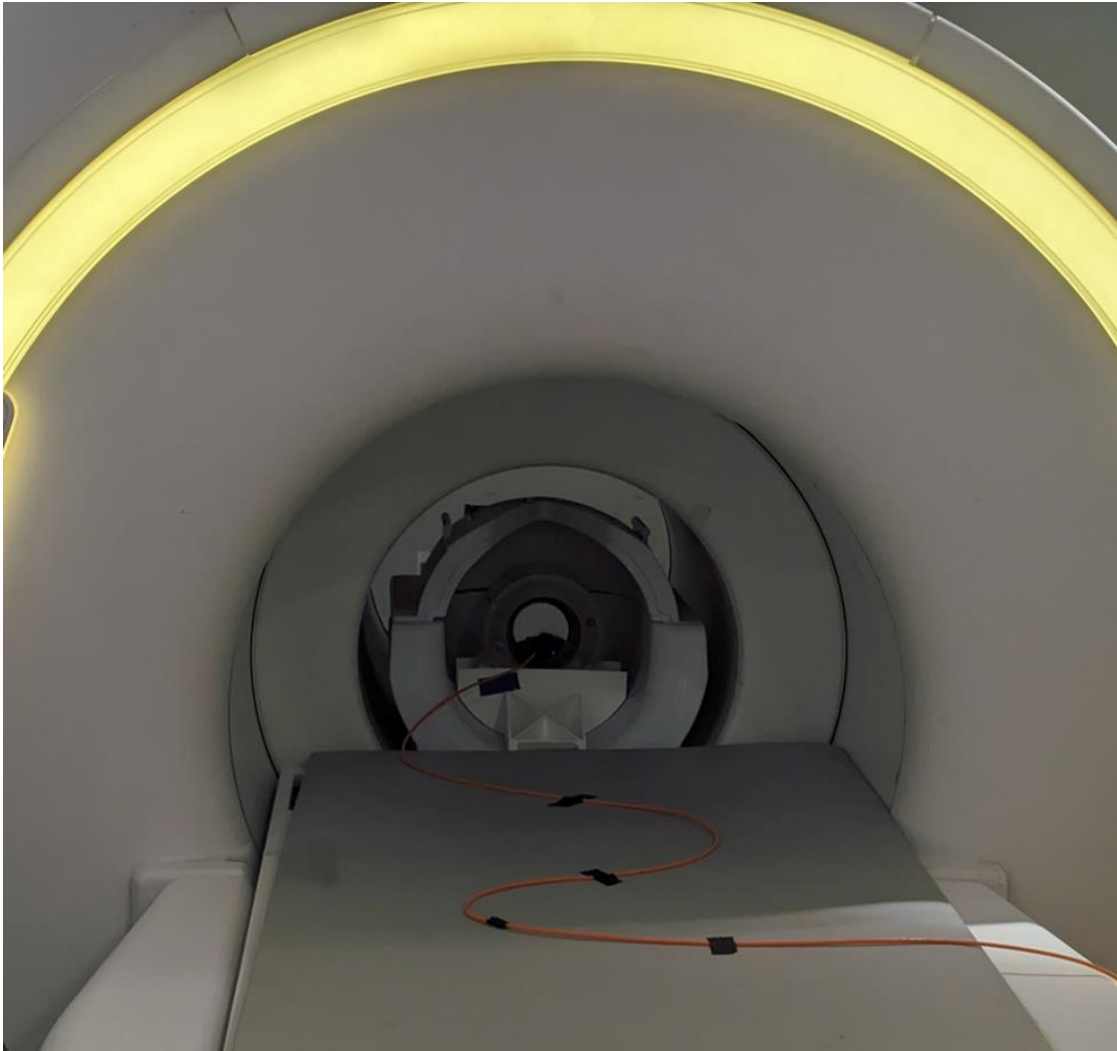


**Figure 3.3:** Photo of experimental set-up

The experiment was done on a 0.5 T head only scanner, using an 8-channel RF head coil. Fibre optic temperature probe was connected through a waveguide to a NOMAD touch [Qualitrol] system, kept outside of the MR suite. Inner container of HEC gel was heated using a water bath and the overall phantom was placed in the isocenter of the magnet using a custom 3D printed holder.

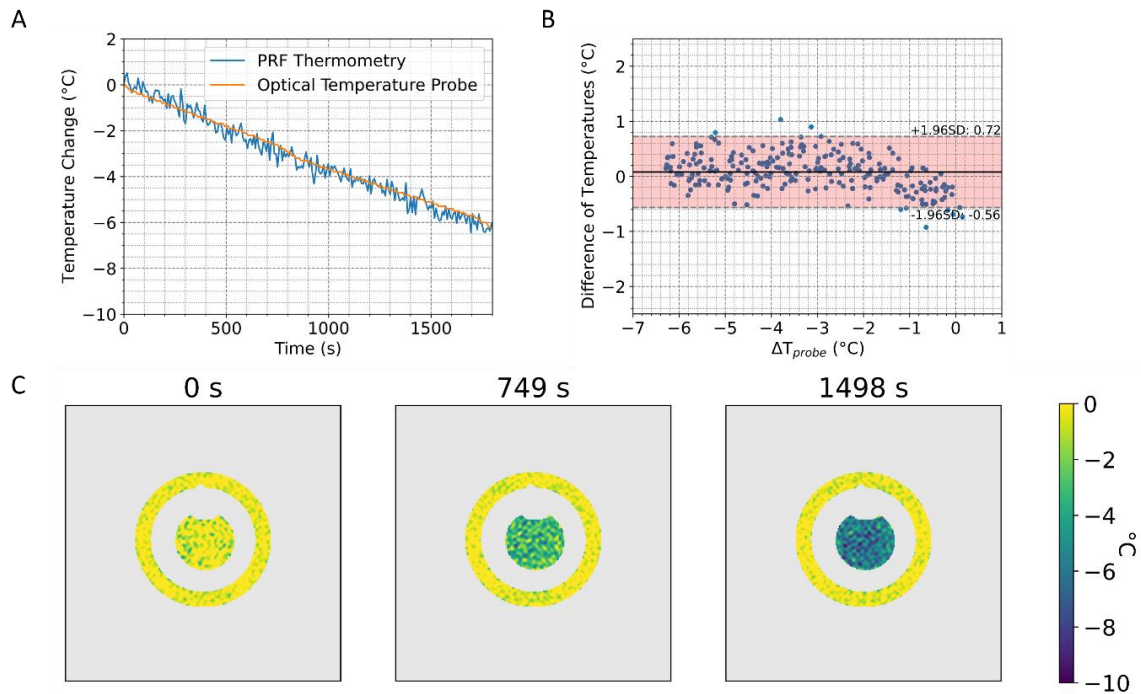


**Figure 3.4:** Relative Temperature change, SE-GRE

(A) using a 3-Slice Single Echo GRE-PRF sequence over a  $1 \times 1 \text{ cm}^2$  region (Blue) and a fibre optic temperature probe placed near the ROI (Orange), (B) a Bland-Altman plot of the temperature variations between the probe and MR measurements. Measurements conducted on a custom HEC gel temperature phantom. Single Echo parameters shown in **Table 3.1**. (C) shows three temperature maps at different time points during cooling, displaying the steady temperature of the reference region, while the cooling region changes.

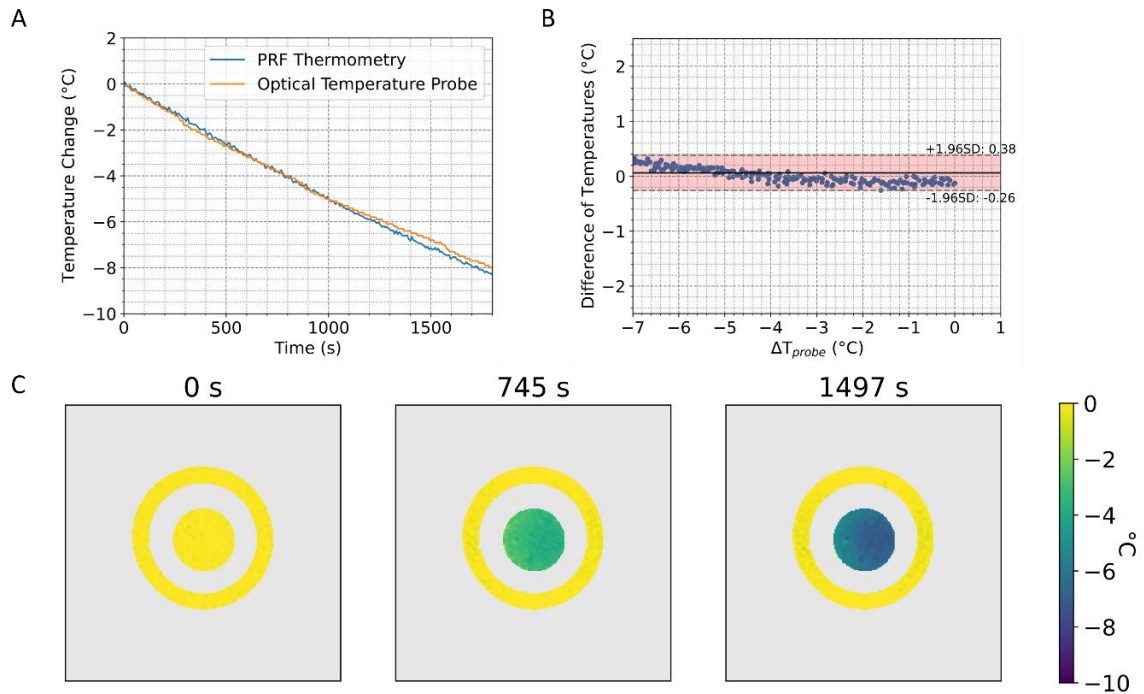


**Figure 3.5:** Relative Temperature change, 3-slice EPI

(A) Relative Temperature change using a 3-Slice EPI-PRF sequence over a  $1 \times 1 \text{ cm}^2$  region with parameters listed in **Table 3.1** (Blue) and a fibre optic temperature probe placed near the ROI (Orange), and (B) a Bland-Altman plot of the temperature variations. Measurements conducted on a custom HEC gel temperature phantom. 22 averages taken in the EPI acquisition to achieve a similar update rate as the 3-slice SEGRE protocol. (C) shows three temperature maps at different time points during cooling, displaying the steady temperature of the reference region, contrasted with the steadily cooling inner region.

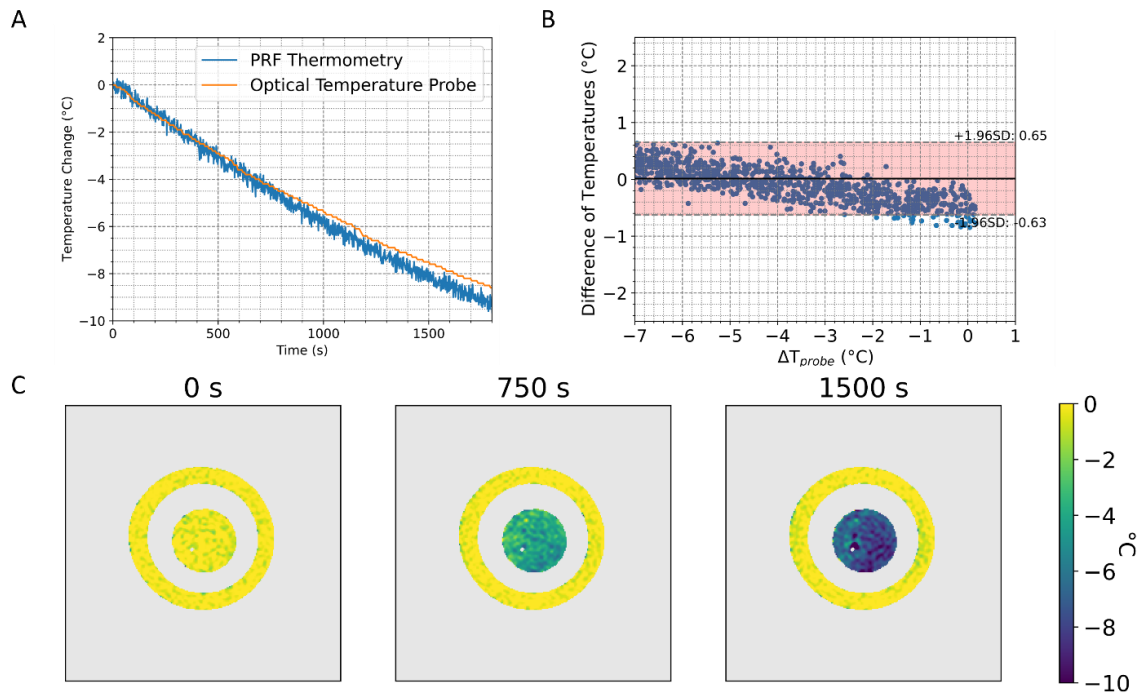


**Figure 3.6:** Relative Temperature change, 13-slice EPI  
 (A) Relative Temperature change using a 13-Slice EPI-PRF sequence over a  $1 \times 1 \text{ cm}^2$  region with parameters listed in **Table 3.1** (Blue) and a fibre optic temperature probe placed near the ROI (Orange), and (B) a Bland-Altman plot of the temperature variations. Update rate of 1.508s, with no averaging of time points. (C) shows three temperature maps at different time points during cooling, displaying the steady temperature of the reference region, while the cooling region changes.

### 3.4 Discussion

Production of the two-cylinder phantom for use in thermal tracking provided some benefits compared to a more common water bath approach seen in many thermometry phantom experiments. Having two regions thermally separated by the foam layer between allows for a stable reference temperature in the imaging region which can be measured/tested and monitored with a reference temperature probe. The heated sample tube being replaceable in the molded foam allows for quick subsequent temperature mapping experiments with little downtime. The sample tube provided a relatively large imaging region, which would be combined with different temperature therapy methods to evaluate heating localization. One of the strengths of using HEC, as the gelled saline is viscous enough to limit the convective transport of heat. This offers the potential ability to measure heat accumulation of thermal therapies in the phantom gel.

In tracking within a phantom, the experiment has shown effective abilities using SE-GRE at a magnetic field strength of 0.5 T. However, we've observed a notable leap in performance when using EPI, where the tracking accuracy is significantly improved at a similar update rate. From **Figures 3.4 and 3.5**, the uncertainty in temperature tracking from Bland-Altman plots, even with some temperature drift provided a smaller uncertainty in the tracking using EPI, suggesting that should a 7.6 s update rate be acceptable, the EPI approach provides a better option for a PRF thermometry implementation.

The SE-GRE approach provided a 1.3°C temperature uncertainty using the 95% confidence interval. One of the major concerns revolves around the update rate necessary for real-time temperature measurement in an in vivo setting. If the intent is to provide real time tracking for interventional temperature tracking, a key challenge in using a SEGRE-based method is increasing the update rate while improving coverage. As the experiment conducted used an update rate of 7.8 s over 3 slices and 9 cm slice coverage, this may be sufficient for application, however any additional slices added on will decrease the update rate.

To address this update rate challenge, we have explored the possibility of implementing a sub-2-second update rate by utilizing a single time point on a full coverage EPI sequence. With a 1.508 second update rate, the EPI sequence produced a similar uncertainty to the small coverage single echo approach, while exhibiting an update rate over 5 times faster. Evaluating the trade-off between time efficiency and information gain will be critical in optimizing this approach, as a  $\sim 1.5$  s rate may be unnecessarily fast for interventional application, so increasing the number of averages may be of interest to find a balance of uncertainty and temporal resolution.

From these update rates, the clinical viability of our experiment is robust even when pushing the boundaries at 0.5 T. Despite employing echo times that deviate from optimal settings in the single echo case, we have maintained an uncertainty of around 1.25 degrees in temperature tracking. This leads us to infer that the 0.5 Tesla field strength allows for a certain level of flexibility without compromising the overall effectiveness of the experiment, even when using a simple single echo approach.

Depending on application, the update rate shown in the SE-GRE approach is acceptable, particularly in pelvic region where motion artifacts will not significantly affect the image [26,27], or when imaging under breath hold conditions where clinical expectations are to balance parameters such that images are acquired under 15-20s, such as in treatment of liver tumors [28]. In the cases where real-time imaging is the goal [21,22,27], or for patients who cannot do breath hold imaging, there is motivation to use the faster EPI methods, where there is also flexibility to improve temperature measurement precision by increasing the number of averages to match the target update rate.

### 3.5 Conclusion

Temperature mapping using PRF based approaches on a mid-field cryogen-free MR scanner using both single echo GRE and EPI were compared. Using two comparisons, EPI-PRF was shown to outperform the SE-GRE PRF, as in vivo the EPI based approach showed better temperature precision in the brain when both methods used similar acquisition times.



Further, when comparing temperature tracking in a phantom using a Bland-Altman plot, the temperature confidence intervals for the EPI implementation were smaller than when tracked using the single echo method. Also, an optimized full coverage EPI sequence matched the SE-GRE temperature precision while providing a 5x faster update rate.

## 3.6 References

- [1] Odéen, H. & Parker, D. L. Magnetic resonance thermometry and its biological applications – Physical principles and practical considerations. *Prog Nucl Magn Reson Spectrosc* **110**, 34–61 (2019).
- [2] Rieke, V. & Pauly, K. B. MR thermometry. *Journal of Magnetic Resonance Imaging* **27**, 376–390 (2008).
- [3] Leopold, K. A. *et al.* Cumulative minutes with T90 greater than tempindex is predictive of response of superficial malignancies to hyperthermia and radiation. *International Journal of Radiation Oncology\*Biophysics* **25**, 841–847 (1993).
- [4] Kim, Y., Rhim, H., Choi, M. J., Lim, H. K. & Choi, D. High-intensity focused ultrasound therapy: an overview for radiologists. *Korean J Radiol* **9**, 291–302 (2008).
- [5] Huber, P. E. *et al.* A new noninvasive approach in breast cancer therapy using magnetic resonance imaging-guided focused ultrasound surgery. *Cancer Res* **61**, 8441–8447 (2001).
- [6] Jolesz, F. A. & McDannold, N. J. MRI-guided focused ultrasound. in *Intraoperative Imaging and Image-Guided Therapy* 403–412 (Springer, 2014).
- [7] Peliowski-Davidovich, A., Society, C. P. & Committee, F. and N. Hypothermia for newborns with hypoxic ischemic encephalopathy. *Paediatr Child Health* **17**, 41–43 (2012).
- [8] Tagin, M. A., Woolcott, C. G., Vincer, M. J., Whyte, R. K. & Stinson, D. A. Hypothermia for Neonatal Hypoxic Ischemic Encephalopathy: An Updated Systematic Review and Meta-analysis. *Arch Pediatr Adolesc Med* **166**, 558–566 (2012).
- [9] Douglas-Escobar, M. & Weiss, M. D. Hypoxic-Ischemic Encephalopathy: A Review for the Clinician. *JAMA Pediatr* **169**, 397–403 (2015).

- [10] Lemyre, B. & Chau, V. Hypothermia for newborns with hypoxic-ischemic encephalopathy. *Paediatr Child Health* **23**, 285–291 (2018).
- [11] Campbell-Washburn, A. E. *et al.* Opportunities in interventional and diagnostic imaging by using high-performance low-field-strength MRI. *Radiology* **293**, 384–393 (2019).
- [12] Stainsby, J. A. *et al.* Imaging at 0.5 T with high-performance system components. *Proc 27th Annu Meet ISMRM Montr Canada* (2019).
- [13] Connell, I. R., Panther, A. & Chronik, B. A. Specific Absorption Rate in Head-Only Mid-Field Scanner: Comparisons to 1.5 T and 3 T. in *Proc Intl Soc Mag Reson Med* vol. 27 4167 (2019).
- [14] Shepherd, S. *et al.* Optimized, Minimal Specific Absorption Rate MRI for High-Resolution Imaging in Patients with Implanted Deep Brain Stimulation Electrodes. *American Journal of Neuroradiology* **37**, 1996–2000 (2016).
- [15] Webb, A. & O'Reilly, T. Tackling SNR at low-field: a review of hardware approaches for point-of-care systems. *Magnetic Resonance Materials in Physics, Biology and Medicine* 1–19 (2023) doi:10.1007/S10334-023-01100-3/FIGURES/8.
- [16] Fiorito, M., Yushchenko, M., Cicolari, D., Sarracanie, M. & Salameh, N. Fast, interleaved, Look-Locker-based T1 mapping with a variable averaging approach: Towards temperature mapping at low magnetic field. *NMR Biomed* **36**, e4826 (2023).
- [17] Harris, C. T. *et al.* 2D Imaging near Metallic Implants at 0.5T using High Time-Bandwidth Product RF pulses. in *ISMRM 27th Annual Proceedings* (2019).
- [18] Blackwell, J. *et al.* Proton Resonance Frequency Shift Thermometry: A Review of Modern Clinical Practices. *Journal of Magnetic Resonance Imaging* **55**, 389–403 (2022).
- [19] Ishihara, Y. *et al.* A precise and fast temperature mapping using water proton chemical shift. *Magn Reson Med* **34**, 814–823 (1995).

- [20] Kickhefel, A. *et al.* Clinical evaluation of MR temperature monitoring of laser-induced thermotherapy in human liver using the proton-resonance-frequency method and predictive models of cell death. *Journal of Magnetic Resonance Imaging* **33**, 704–709 (2011).
- [21] Stafford, R. J. *et al.* Interleaved echo-planar imaging for fast multiplanar magnetic resonance temperature imaging of ultrasound thermal ablation therapy. *Journal of Magnetic Resonance Imaging* **20**, 706–714 (2004).
- [22] Cernicanu, A., Lepetit-Coiffe, M., Roland, J., Becker, C. D. & Terraz, S. Validation of fast MR thermometry at 1.5 T with gradient-echo echo planar imaging sequences: phantom and clinical feasibility studies. *NMR Biomed* **21**, 849–858 (2008).
- [23] Lee, G. C. *et al.* Pyrolytic graphite foam: A passive magnetic susceptibility matching material. *Journal of Magnetic Resonance Imaging* **32**, 684–691 (2010).
- [24] International Organization for Standardization (ISO). Assessment of the safety of magnetic resonance imaging for patients with an active implantable medical device. (2018).
- [25] Rieke, V. *et al.* Referenceless MR thermometry for monitoring thermal ablation in the prostate. *IEEE Trans Med Imaging* **26**, 813–821 (2007).
- [26] Łoziński, T., Filipowska, J., Gurynowicz, G., Gabriel, I. & Czekierdowski, A. Non-invasive therapeutic use of High-Intensity Focused Ultrasound (HIFU) with 3 Tesla Magnetic Resonance Imaging in women with symptomatic uterine fibroids. *Ginekol Pol* **88**, 497–503 (2017).
- [27] Holbrook, A. B., Santos, J. M., Kaye, E., Rieke, V. & Pauly, K. B. Real-time MR thermometry for monitoring HIFU ablations of the liver. *Magn Reson Med* **63**, 365–373 (2010).

- [28] Rempp, H., Clasen, S. & Pereira, P. L. Image-based monitoring of magnetic resonance-guided thermoablative therapies for liver tumors. *Cardiovasc Intervent Radiol* **35**, 1281–1294 (2012).

## 4 Challenges Facing Implementation of Thermal Mapping using MRI

Having established approaches for thermal mapping, we now turn our attention to evaluating some of the concerns that MR systems have when not placed in specialized rooms with faraday cages and specific room architectures, have. This includes looking at the effects of mass metal motion, strong gradient operation, and quench behavior at ramped down field strengths.

### 4.1 Introduction

In recent years, the Magnetic Resonance (MR) field has seen a renewed focus on the proliferation of lower field and accessible MR systems [1–6]. These modern systems are designed to simplify the setup process and reduce costs, allowing for a departure from the traditional "4 zone" approach in MR room design. Along with the aim of improving access to MRI, these systems are meant to be used in non-traditional situations such as clinics and surgical suites where specialized MR sequences can be used for interventional treatment of various ailments [4].

Developments which aim to reduce the footprint needed for an MR have necessitated the development of cryogen-free MR systems which do not require the use of large quantities of cryogen to keep the main magnet at a superconducting temperature [1,7]. This avoids managing the need for cryogen venting set up in the case of a loss of main magnet superconductivity; called a quench and enabling placement of MR systems in these atypical locations [8]. Such design advancements allow for relatively quick adjustments to the main magnetic field strength without the traditional challenges associated with helium boil-off. Such advancement has opened doors to new and unexplored applications in MR imaging at several field strengths to take advantage of changing tissue properties at different field strengths [5,6]. Moreover, there is an opportunity to capitalize on reduced susceptibility artifacts [4], along with increased dynamic range [9] in the mid-field.

This focus on interventional MR systems comes with its own set of challenges, particularly in terms of maintaining sufficiently high field stability [10]. The reduction in footprint and subsequent simplification of MR room design comes at the cost of MR scanners being nearer to objects which could disturb the magnetic field generated by the system. While this reduced footprint approach can make MR systems more practical in a wider range of settings, it raises concerns about the impact of these disruptions on applications that rely on a stable magnetic field for extended periods of time [2,11]. Some common metallic objects which could affect the magnetic field include elevators, gurneys, and passing motor vehicles. The effect of these dynamic sources of field disturbances are usually mitigated due to the typical architecture in imaging departments, as these dynamic sources cannot be easily corrected using conventional methods like shimming, which adjusts the magnetic field to counteract static distortions [10].

Evaluating the effects that these sources present has typically been done using low-precision magnetometers to analyze the magnetic fields over time. These studies primarily explore how the resulting distortions can be used to determine the localization of the objects [12,13]. However, little attention has been given to the potential impact of these distortions on the main magnetic field of the MR scanner itself; and the subsequent imaging.

Along with protecting stability and preventing distortions, ensuring the operational safety of these systems is critical. In the case of an emergency, MR systems have mechanisms in place which can eliminate the strong magnetic field in several seconds, which is necessary for emergency response teams to safely approach the bore of the magnet (with ferromagnetic equipment) to aid a patient in an emergency [3,8]. This process involves heating specific sections of the superconducting coils above critical temperature ( $T_c$ ) at which point they become non-superconducting. This region, which now has a resistance, will further heat which propagates non superconductivity and can quickly snowball to make the entire magnet non-superconducting if not controlled [14,15]. Controlling this

process allows the non-superconducting region to propagate in a safe and well-defined manner, protecting the MR components from damage.

With systems which can be run at different magnetic field strengths, a variable field requires adaptations in the quench method to ensure quick field removal. The critical temperature of each coil in the magnet is affected by the field the system is set at, and this affects the amount of energy required to heat the windings above the superconducting threshold temperature [14]. Passive quench protection circuits must be designed to operate at the lowest current the magnet is expected to be run at, as it is a priority to ensure the magnet itself is not damaged by the heating which occurs in the magnet coils during this process [16,17].

As designs of cryogen-free MR systems have evolved, a major aim has been to bridge the gap in image quality when compared to typical 1.5T systems and producing high-quality images comparable to those acquired using these higher field strength scanners [10]. When equipped with state-of-the-art gradient and radiofrequency (RF) components, these systems can bridge the signal to noise ratio (SNR) gap and provide similar image quality to their higher field counterparts while reducing some of the costs that are typically associated with the set up and maintenance of a clinical MRI scanner [3,4]. Alongside this, the use of a lower main magnetic field has been shown to reduce the Specific Absorption Rate (SAR) when performing RF excitations, consistent with the fundamental  $SAR \propto B_0^2$  relation [18]. This reduction in energy deposition allows for gradient strength limits to be alleviated, with the gradient run more powerfully to improve image resolution.

The absence of a substantial cryogenic liquid helium reservoir introduces an intriguing thermal-handling challenge. With cryogen-free systems, maintaining precise temperature control becomes difficult, particularly in the presence of gradient-induced eddy current heating. This phenomenon arises due to the interaction between the rapidly changing magnetic fields produced by the gradient coils and the conductive surfaces in the MR system [19]. Conventional cryogenic systems are able to regulate coil temperature more robustly due to the entire MR system being effectively submerged in liquid helium. The



absence of a substantial cryogen heatsink means cryogen-free designs are less resistant to induced heating. This becomes especially relevant as gradient strength increases, such as in modern research-oriented gradient systems designed for head imaging whose gradients can approach 200 mT/m [3].

While methods like pre-emphasis and post-processing can correct gradient-induced eddy current fields, a significant concern remains: the potential heating of the magnet during imaging sequences. This heating could lead to field instability or produce a quench in more extreme cases. Existing research has already demonstrated how the thermal handling characteristics of cryogen-free MRI magnets can impact the stability of the main magnetic field [15].

This study aims to delve into the challenges facing the use and implementation of interventional MRI systems in non-traditional locations. Particularly addressing the effect of mass metallic motion, the behavior of quench dynamics on variable field strength magnets, and the effect of gradient coil operation on the primary magnet system. By shedding light on the dynamics both within the magnet systems and between the magnet and the environment, this research contributes to improving applications using accessible MRI systems.

## 4.2 Methods

### 4.2.1 Measurement of magnetic field disturbances

Measurement of magnetic field information in the case of an elevator operating was collected using a 3-axis fluxgate probe with calibration range 0-100  $\mu$ T (Metrolab THM1186). The sampling rate of the probe was set to 100 points per second, and a 50-point rolling average was performed to reduce the noise in the measurements, also providing a standard deviation. Both passenger elevator and a cargo elevator were used in this study. A time series was acquired while the elevator was taken to each floor in order, producing a record of the field changes relative to the initiation of data collection. This process was repeated for all 6 positions on all the accessible floors for both elevators. Time

series information was analyzed in Python, with the maximum field change determined at for each floor and at 5 distances from the elevator. The maximum field change as a function of distance was fit to a  $1/r^3$  function to match a gross approximation of the elevators as magnetic dipoles.

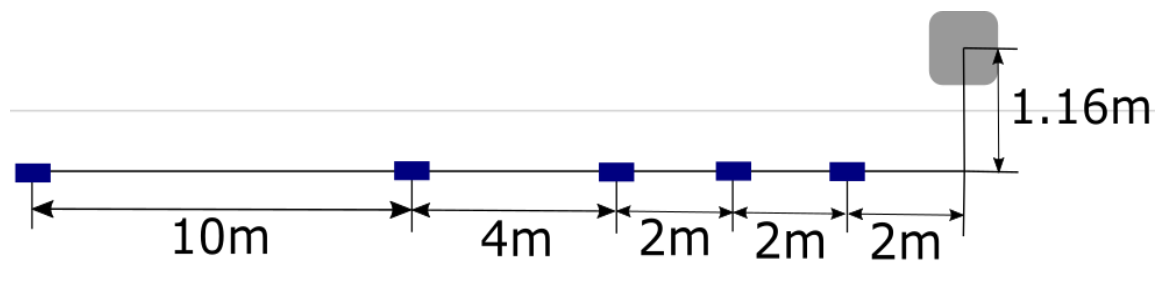


**Figure 4.1:** Schematic of elevator probe location set up, with each spot being a measurement location.

#### 4.2.2 Quench evaluation at variable field strengths

Quench dynamics were investigated using a calibrated magnetic field probe placed at the isocenter inside the bore of a cryogen-free superconducting magnet designed to operate at a maximum field of 0.5 T at 101 A. The field probe voltage output and the voltage of the quench circuit were recorded with a data acquisition system (National Instruments), using a custom LabVIEW program, with data collection occurring until recorded field had settled to less than 5 Gauss. Ten quenches were conducted with current varying between 10 A and 101 A (maximum current). The analysis of the quench was done using custom Python code to optimize a fit using a plateaued difference of exponentials to model the behaviors of the main field coils and the shielding coils. The model of the quench was then used to test the predicted settling time (time elapsed until the measured field reached 5 Gauss).

#### 4.2.3 Gradient interaction measurement

The temperature dynamics were investigated using a set of 7 temperature probes placed throughout the main and shield coils of a compact cryogen-free superconducting magnet located in our labs designed to operate at a field of 0.5 T. The temperature probe voltage outputs were exported using an NI DAQ system, using a LabVIEW program to collect data

for 400 seconds. A prototype asymmetric gradient coil designed for head-only imaging with this magnet was connected to a gradient amplifier capable of 900 A peak current. Two gradient pulse sequences were tested using the different gradient components. First, single long trapezoidal pulse mimicking use in a diffusion imaging sequence was used, with a rise time of 0.1 ms and a duration of 100 ms, subsequently repeated. Secondly, a series of bipolar trapezoidal lobes mimicking an echo planar imaging train with trapezoids having duration 30ms, cycling lobes. Maximum gradient amplitudes we measured at 65 mT/m and 130 mT/m.

A comparison of heating induced by the different gradient axes was used to determine which had the largest heating effect by comparing heating after 400 s of gradient operation. Using these results, the axis producing the strongest interactions was compared to itself at different gradient strengths. The analysis of the temperature shift was done using MATLAB and Python to fit a model to the effect of varying gradient strength on the temperature of the main magnet over the duration of the gradient operation. The heating model was used to describe the predicted settling time (time until the temperature reached equilibrium).

### 4.3 Results

To measure the effect of mass magnetic motion, magnetic field measurements were collected throughout an elevator operation cycle, with an annotated time series shown in **Figure 4.1**, highlighting the change of floors as the elevator cycles, as well as the confidence intervals due to the rolling average taken. The  $1/r^3$  fit is shown in **Figure 4.2** for data from a passenger elevator and cargo elevator, along multiple distances from the doors of the elevator, with the cargo elevator displaying lesser field variations at similar distances.

In evaluating field dynamics for a set of quenches from 60A to 101A, **Figure 4.3** displays the series of quench behaviours at a series of currents flowing through the main magnet coils. To show the time it takes to reach the 5-Gauss safety line, **Figure 4.4** displays the

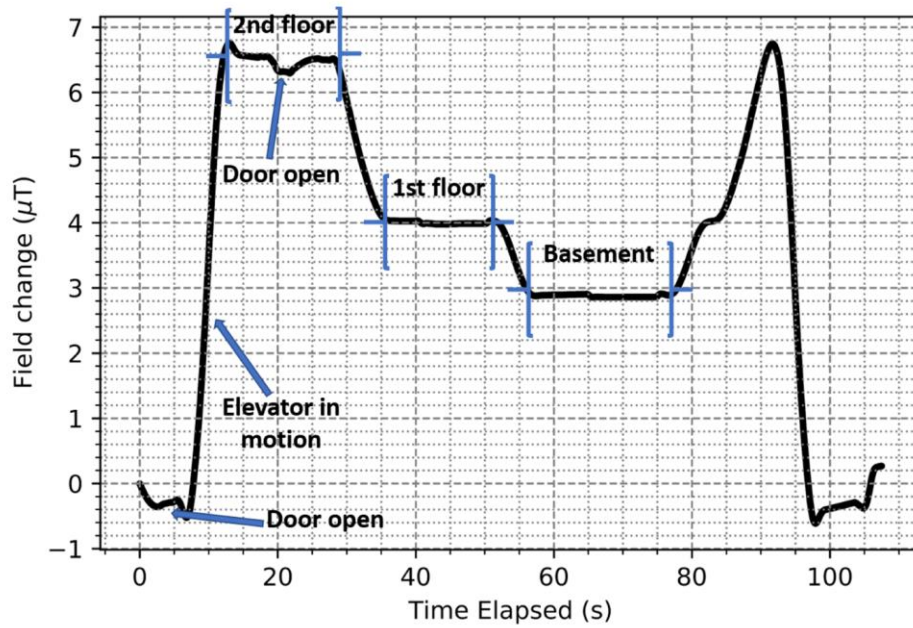


**Figure 4.2:** Graph of a sample time series from the passenger elevator Measured from the highest floor position of the elevator, 1.16m from the elevator door. The field change was measured relative to the initial field as the elevator cycled through the floors and ultimately returned to the top. From these measurements, the maximum field change was extracted and used to compare at distances from the elevator.

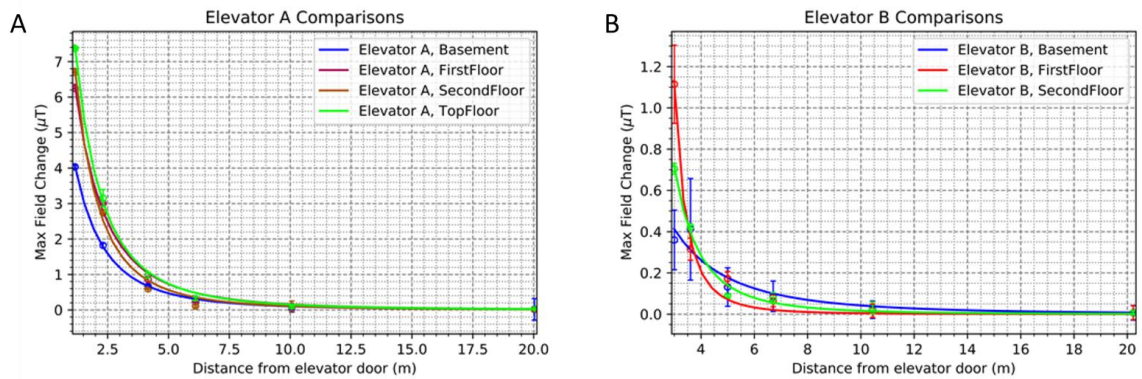


**Figure 4.3:** Graph displaying the maximum field change due to elevators Measured on a passenger elevator (**A**) and a cargo elevator (**B**) compared to the distance from the elevator door. The data follows an inverse cubic relationship in all cases, as can be seen in A where the shape remains consistent throughout the entire length. There is more variability in the field measured in the second elevator experiment, due to differences in elevator model and local environment near the elevator.

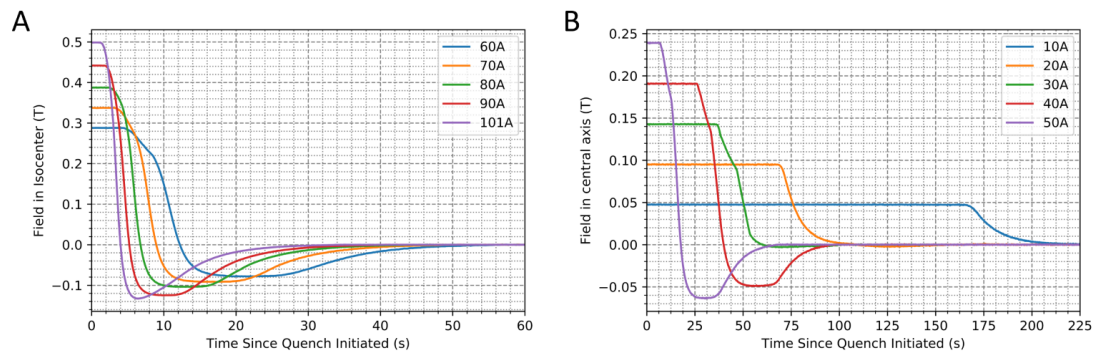


**Figure 4.4:** Set of field measurements for quenches at a series of field strengths Initial field strengths correspond to an initial current flowing through the main magnet windings. Figures are split into a set of higher currents (**A**), and lower current set (**B**). The initial field in the central axis is initially determined by the amount of current flowing through the system, with a reverse field seen in quenches between 40A and 101A, along with a delay in quench initiation at lower initial currents.

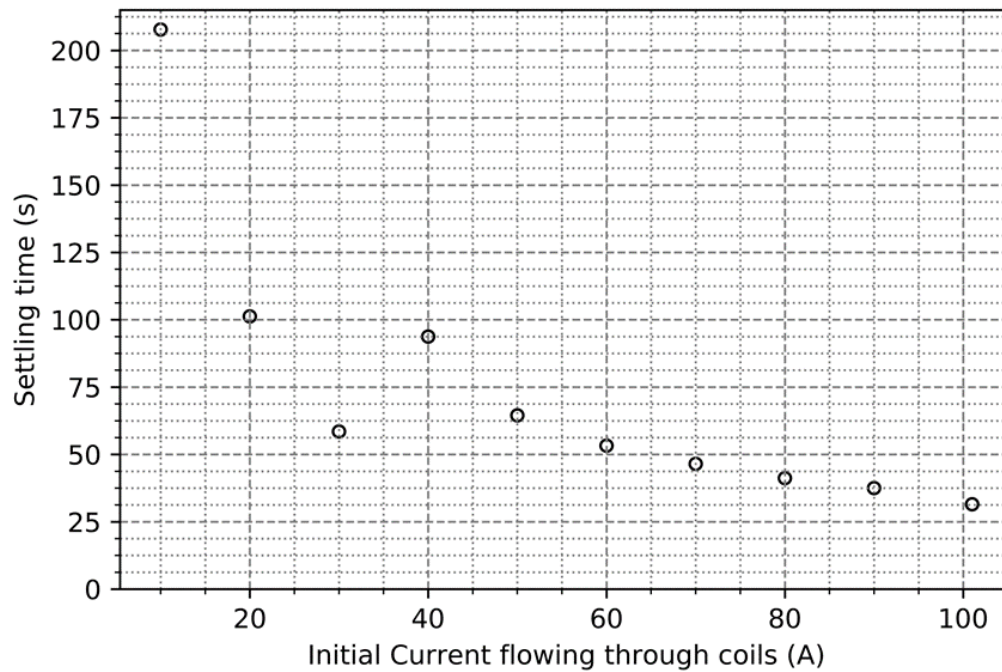


**Figure 4.5:** Plot of the quench settling time

Time plotted is the time required for the field in the central axis where field probe was located to reach the 5 Gauss safety level, shown at different initial current flowing through the main magnet windings. Two regimes can be seen, one above 40 A and one below, where the shield coil delays the time taken before the field measured in the isocenter of the magnet bore reaches this threshold. The delay in this low current regime seems to rise from the propagation of the quench onto the shield coils at the same rate as the main coil windings.

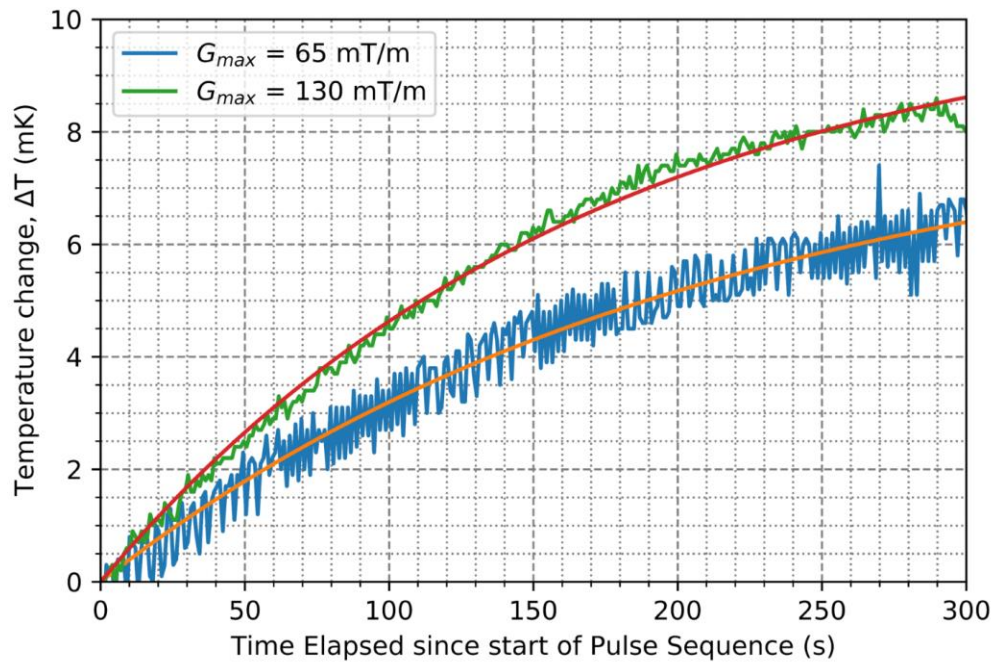


**Figure 4.6:** Time series of magnet temperature heating Measured during x-axis gradient operation with 65 mT/m (blue with orange fit) and 130 mT/m (green with red fit) amplitudes. The gradient was operated as a diffusion pulse made up of a single trapezoid with a rise time of 0.1 ms and a duration of 100 ms, immediately repeated.

Gradient max strength	Temperature Rise (mK)	$\tau$ (s)
65 mT/m	8.28	192.3
130 mT/m	10.6	167.5

**Table 4.1:** Summary of results of a gradient heating experiment, with fit used of  $A(1-e^{-x/\tau})$  from **Figure 4.6**, with time constant  $\tau$  the characteristic settling constant guiding time the magnet coils take to reach steady state.

settling time to this 5-Gauss level is shown as a function of the initial current through the coils in both a higher and lower current range, with a change in regime seen between 30 A and 40 A.

The magnet temperature dynamics for a repeated diffusion gradient pulse described in the methods while along with the fit performed are shown in **Figure 4.5** for a 65mT/m maximum gradient and a 130 mT/m maximum gradient. The parameters including the time constant determined through fitting the heating curves is shown in **Table 4.1** for the diffusion pulse, with derived time constant 192.3 s for the 65 mT/m trial and 167.5 s for the 130 mT/m run.

## 4.4 Discussion

The aim of the experiments carried out was to test the behaviours that exist when an MR system is placed nearer to sources of magnetic instability, as well as determining what concerns could arise when running the system more intensely to compensate for the reduced SNR at lower field strength.

In testing the effect of operating the magnet near an elevator as a proxy for other large magnetic objects (e.g., vehicular traffic near an emergency room), the expected fit showing  $r^{-3}$  behaviour was verified, suggesting that in terms of modelling and predicting the effects that a system could be exposed to, a magnetic dipole approximation is appropriate. This approximation is limited to predictions using a dipole past 5m from the elevator door. In general, the effect on field was in the order of 1000 nT at ~5 m, 100 nT at ~10 m, and 10 nT at ~20 m. From this knowledge, it appears unlikely that an elevator will distort the



static field of an MR system in a noticeable manner, provided it is located more than 10 m away.

Typically, it is only the field oriented in the axis of the magnet that will affect imaging, and the current through the superconducting coils will flow to compensate for a changing magnetic flux should there be a changing field. These factors suggest that unless the induced field happens to be in the direction of the main magnetic field, the effect of the distorting field would be significantly less than this worst-case total field shift. Regardless, at the field of a mid-field scanner operating at 0.5 T, the field shift at 10 m would correspond to a ppm shift in the proton frequency of less than 0.2 ppm, suggesting that the effect that this shift will not likely affect the image quality of an acquisition at this distance.

When it comes to room placement, this experiment demonstrates the need to continue to consider the sources of dynamic instability that can occur near to a magnet. Shimming conducted before a scan cannot consider the mobile movement and change in the local magnetic environment, and this change could result in some shifts. A large focus in the siting of these MR systems concerns the range and location of the 5-Gauss safety line, as this is an important safety boundary for clinicians and researchers interacting with the system. This work suggests that a secondary siting requirement should be to still implement elements of the 4-zone architecture, with consideration made to keeping mass metallic objects far from the magnet to ensure quality of scanning.

In dealing with a sudden loss of field during a quench, a difference of exponentials fit was found as a suitable model of the dynamics of the quench behaviour observed. Lower standard deviation suggests that the fit is effective at the ends of the current range, and it is hypothesized that the delays in propagation of the quench results in a less accurate fit in some of the trials. Importantly, the study showed that the time taken to quench the system increases as the starting field is reduced. This increase in settling time is likely due to the increase time it takes for the quench to propagate with a lower current being used at lower

fields. Once resistance is established in the main coils, the lower current causes less heating than when the system is operating with maximum current.

The magnetic field flip observed from the initial orientation is due to the shield coils being the last to quench. Below 40 A, the quench occurs as a single step, simply settling to zero and not reversing field direction. The two regimes of behaviour can be seen with the entire system quenching in one step at lower current, and at higher currents the quench occurring fast enough that the shield coils being the last coil to quench becomes evident in the field measurements. In these cases, this ends up causing the settling time to take longer at 40 A and 50 A than at 30 A.

To improve the settling time in this magnet, the quench circuit could be amended to deposit more heat (so that the delay in quench beginning is reduced) and the heating elements on the shields and primary coils could be better balanced to make the quench simultaneous over the various magnet windings and shield windings. As the priority in an emergency is to access a patient in the scanner, it is important to consider the design of a quench circuit to operate efficiently at all intended field strengths.

As quenches can be manually triggered or spontaneously generated, the study on the potential heating caused by gradient operation on the main magnet provided insight into the potential risks with operating high-performance gradient on a system with dampened cooling capabilities. In the study, the estimated increase in temperature due to this gradient operation was shown to be in the tens of milli-Kelvin, which is not cause for immediate concerns of reaching a critical temperature; where the main magnet ceases to be superconducting. Likely, the gradient coil temperature itself would reach a limit before the induced heating would be a concern, unless the system were already close to the critical temperature  $T_c$ .

A five-minute operation time was sufficient to determine the heating-time constants, which should give some expectation of the total heating potential on the main magnet. In these

cases, there is further concern to be investigated on the effect that induced currents have on the magnet.

## 4.5 Conclusion

The operation of a cryogen free system for interventional purposes is a growing field of study, with both new and legacy companies vying to disrupt the market for mid and low field systems. The experiments carried out here address some of the concerns that exist with these systems and suggest better practices for dealing with a system both in their emergency-quench procedures to ensure faster quench propagation. As well, the risks for heating a magnet to quench temperature due to gradient operation was shown to be unlikely, along with showing that there is low distortion risk for imaging when mass metallic objects are over 10 m away from an MR system.

## 4.6 References

- [1] Manso Jimeno, M., Vaughan, J. T. & Geethanath, S. Superconducting magnet designs and MRI accessibility: A review. *NMR Biomed* (2023) doi:10.1002/nbm.4921.
- [2] Arnold, T. C. *et al.* Sensitivity of portable low-field magnetic resonance imaging for multiple sclerosis lesions. *Neuroimage Clin* **35**, 103101 (2022).
- [3] Stainsby, J. A. *et al.* Imaging at 0.5 T with high-performance system components. *Proc 27th Annu Meet ISMRM Montr Canada* (2019).
- [4] Campbell-Washburn, A. E. *et al.* Opportunities in interventional and diagnostic imaging by using high-performance low-field-strength MRI. *Radiology* **293**, 384–393 (2019).
- [5] Marques, J. P., Simonis, F. F. J. & Webb, A. G. Low-field MRI: An MR physics perspective. *Journal of Magnetic Resonance Imaging* **49**, 1528–1542 (2019).
- [6] Coffey, A. M., Truong, M. L. & Chekmenev, E. Y. Low-field MRI can be more sensitive than high-field MRI. *Journal of Magnetic Resonance* **237**, 169–174 (2013).
- [7] Lvovsky, Y., Stautner, E. W. & Zhang, T. Novel technologies and configurations of superconducting magnets for MRI. *Supercond Sci Technol* **26**, 093001 (2013).
- [8] Kellogg, J. Confronting challenges to urban-based MRI facilities. *DOT Medbusiness News* (2011).
- [9] Campbell-Washburn, A. E. *et al.* Evaluation of Hepatic Iron Overload Using a Contemporary 0.55 T MRI System. *Journal of Magnetic Resonance Imaging* **55**, 1855–1863 (2022).
- [10] Webb, A. & O'Reilly, T. Tackling SNR at low-field: a review of hardware approaches for point-of-care systems. *Magnetic Resonance Materials in Physics, Biology and Medicine* 1–19 (2023) doi:10.1007/S10334-023-01100-3/FIGURES/8.

- [11] Cepek, J., Chronik, B. A. & Fenster, A. The effects of magnetic field distortion on the accuracy of passive device localization frames in MR imaging. *Med Phys* **41**, 052301 (2014).
- [12] Ouyang, G. & Abed-Meraim, K. Analysis of Magnetic Field Measurements for Indoor Positioning. *Sensors (Basel)* **22**, 1–8 (2022).
- [13] Shu, Y. *et al.* Magicol: Indoor Localization Using Pervasive Magnetic Field and Opportunistic WiFi Sensing. *IEEE Journal on Selected Areas in Communications* **33**, 1443–1457 (2015).
- [14] Seo, K., Morita, M., Nakamura, S., Yamada, T. & Jizo, Y. Minimum quench energy measurement for superconducting wires. *IEEE Trans Magn* **32**, 3089–3093 (1996).
- [15] Trillaud, F., Ayela, F., Devred, A. & Tixador, P. Investigation of the stability of Cu/NbTi multifilament composite wires. *IEEE Transactions on Applied Superconductivity* **16**, 1712–1716 (2006).
- [16] Dixon, I. R., Gavrilin, A. V., Miller, J. R., Powell, J. A. & Brandt, B. L. Analysis of the quench protection system of a series connected hybrid magnet. *IEEE Transactions on Applied Superconductivity* **17**, 2446–2449 (2007).
- [17] Poole, C., Baig, T., Deissler, R. J. & Martens, M. Numerical analysis of the coupling loss induced quench protection for a 1.5 T whole-body MgB<sub>2</sub> MRI magnet. *Supercond Sci Technol* **30**, 105005 (2017).
- [18] Connell, I. R., Panther, A. & Chronik, B. A. Specific Absorption Rate in Head-Only Mid-Field Scanner: Comparisons to 1.5 T and 3 T. in *Proc Intl Soc Mag Reson Med* vol. 27 4167 (2019).
- [19] Brown, R. W., Cheng, Y.-C. N., Haacke, E. M., Thompson, M. R. & Venkatesan, R. *Magnetic Resonance Imaging: physical principles and sequence design*. (John Wiley & Sons, 2014).

## 5 Thesis Conclusions and Future Directions

### 5.1 Thesis Overview and Research Questions

This thesis aims to shed light on the implementations of thermal mapping to aid in effective implementation on modern MRI systems, for which the future areas of growth in Canada and beyond are focused on accessibility and interventional application. In many cases, the value proposition for mid and low field scanners is the small footprint, reduced cost, and eased siting requirements. Thus, developing applications on these systems requires taking advantage of changes in tissue properties at lower field strengths and ensuring this system can adequately provide image quality which makes applications clinically impactful.

Thus, chapter 2 of this thesis concerned answering the question of “*What are the ideal properties for a tissue mimicking gel which can be used for testing temperature mapping using a variety of MR imaging methods?*”

With an idea of what would make an appropriate phantom gel for thermal mapping, Chapter 3 focuses on developing a phantom which can be used to evaluate the temperature tracking capabilities of thermometry methods. Then the work focused on creating these thermal maps, judging the trade-offs that occur when implementing thermal mapping sequences on a 0.5 T scanner asking the question “*can we implement an echo planar imaging sequence at 0.5 T which can create accurate temperature maps, particularly compared to established gradient echo approaches?*”

With a comparison made and implementation of both GRE and EPI sequences in hand, the question in Chapter 4 becomes “*what are the concerns when operating a system intended for interventional use in non-traditional locations, both in terms of scanner safety?*”

### 5.2 Summary and Conclusions

Chapter 2 focused on the development and validation of a phantom gel for use in monitoring thermal therapies with MRI. Thermal therapies involve heating tissue to specific temperatures for medical treatments, and accurate temperature monitoring is

crucial, so development on an appropriate substance is key. The study explored the use of Hydroxyethyl Cellulose (HEC) gel doped with Copper (II) Sulfate or Gadobutrol as a tissue-mimicking phantom for testing MRI-based thermometry methods.

It was found that the HEC gel, when doped with appropriate agents, could be made to closely mimic brain T1 and T2 relaxation times, making it suitable for imaging. The gel was calibrated to match the temperature ranges commonly encountered in thermal therapies. Then, we performed temperature calibrations on the two versions of doped HEC gel for use in temperature monitoring with various MRI thermometry methods, including Proton Resonant Frequency, T1, and Apparent Diffusion Coefficient thermometry. Upon completing calibrations, we showed that the versatile phantom gel provides a tool for developing and testing MRI-based temperature tracking techniques.

In chapter 3 the applications of thermal therapies were evaluated, which encompass both heat therapy (hyperthermia) and cold therapy (cryotherapy) for medical treatment, as both therapies offer non-invasive treatment options, reducing complications and patient contact. The research explored the use of a mid-field MR scanner for monitoring these thermal therapies. MR thermometry using the PRF method was employed to track temperatures and compare. The study focused on comparing a single echo gradient echo (SE-GRE) approach with an echo planar imaging (EPI) approach for temperature mapping. The research involves a phantom temperature stability experiment, in-vivo temperature tracking, and temperature map reconstruction. We found that the results indicated that the EPI approach offers better temperature tracking precision, along with a quicker update rate, making it an appropriate candidate for quasi real-time interventional temperature monitoring.

The chapter also discusses the practicality of these methods in clinical settings, considering factors like motion artifacts and breath hold conditions, highlighting the potential of mid-field MRI for thermal therapy monitoring and suggesting that future EPI-based approaches may enhance precision in temperature tracking.

Finally, in chapter 4 we explored the challenges facing systems that do not use large cryogen quantities to maintain superconductivity. While making MR placement in unconventional locations feasible and enabling quick adjustments to the main magnetic field strength, this focus on accessibility and interventional use poses challenges related to maintaining high field stability. This study investigated the challenges of implementing interventional MRI systems in unconventional locations like clinics without specialized rooms, addressing the impact of mass metallic motion, quench dynamics at variable field strengths, and gradient coil operation on the main magnet system. Magnetic field disturbances near elevators were measured, along with evaluating quench dynamics at different field strengths. Lastly, main magnet temperature dynamics during gradient coil operation was tested.

The results suggested that elevators have an impact on static magnetic fields, minimized when the systems are located more than 10 meters away. It emphasized the importance of considering dynamic instability sources during room placement and maintaining a safety boundary around the magnet. Quench dynamics indicated that lower field strengths increase settling times during a quench, requiring adjustments to quench circuits for efficient operation at all intended field strengths. Gradient coil operation was found to induce minor heating but posed no serious risk to the superconducting magnet triggering a quench. We addressed challenges and provided recommendations for the operation of cryogen-free MRI systems for interventional purposes.

### 5.3 Future Directions

This thesis represents steps towards implementing applications which are commonly done on higher field systems, and showing how improvements can be made and approached differently at lower field strengths. It also establishes novel methods for producing a tissue mimicking gel which can not only be used for the testing of thermal mapping but can also be used for general MR application testing. In this vein, the outlook for this work is expansive on these fronts.



### 5.3.1 Expanded use of doped HEC

Given its established uses in the device testing community HEC gel widely used, however does not have widespread adoption in the thermal mapping community. As covered in Chapter 2, when doped with Copper (II) Sulfate or Gadobutrol, the relaxation times can be made to match tissue, something which is not the concern of applications in device testing, as these are more interested in the electrical properties and thermal conductivity that HEC provides.

As application testing in the mid-field strength grows, there is space to use this tissue mimicking gel, in the space that it can be used to conduct optimization of sequence parameters before use in applications such as  $T_{1\rho}$  imaging or fMRI. HEC gel was shown to be flexible in formulation, and depending on the uses required, the 2% formulation would be viable should a study require a gel more closely mimicking blood instead of averaged tissue.

### 5.3.2 Thermal mapping with Diffusion Imaging and $T_1$

The Synaptive MR system has demonstrated ability to perform diffusion weighted imaging, and alongside this, the results of measuring the change in temperature in gel with ADC measurements has shown promise, as the temperature response had excellent linearity. This suggests that there is potential for the use of ADC based thermometry, particularly in locations where motion can be minimized to prevent any artifacts from affecting image quality. Likewise, in cryotherapy, the use of  $T_1$  based thermometry showed potential, as this avoids the non-linear response to temperature that appears at or above 50°C. testing and expanded use in this lower field region also avoids any potential for the HEC gel to degrade in quality from being exposed to multiple heating cycles, as this remains a concern even without having seen this effect manifest in heating cycles to 60°C+.

### 5.3.3 Further effects of mass motion and nearby construction

Through discussion with colleagues at conferences, particularly in the low field world, multiple researchers have noted the effects that the building I-Beams or nearby labs have on their MR system. It seems that this is a problem that many have, and an expansion to exploring the effect that construction crews or parking garages (things which are quite common near clinics) could provide some insight into the total magnet stability risk exists when imaging in these sites. The effect seen in the study provides good guidance and should be sufficient to minimize risks for interference with a magnet, however many times once the magnet is sited, construction may happen beyond the control of the operator. Thus, some further investigation into these effects seem to have some potential for fruitful study.

## Appendices

### Appendix A: Phantom Development for Comparison of Thermal Mapping

In the process of creating a viable phantom for temperature mapping, an iterative process involves prototyping. As part of that process, an initial version of the thermal phantom was created which aimed to bring ability to homogenate the temperature within a doped solution after applying a thermal dose using a resistor.

This appendix is a reprint of the peer reviewed conference abstract:

Diego F. Martinez, Curtis N. Wiens, Amgad Louka, Dereck Gignac, Will B. Handler, and Blaine A. Chronik. *Phantom Development for Comparison of Thermal Mapping*. International Society for Magnetic Resonance Imaging Annual Meeting 2022.

#### Introduction:

The non-invasive and tissue dependent nature of Magnetic Resonance (MR) as an imaging modality provides several opportunities for unique applications [1]. MR provides stellar soft tissue contrast and can highlight tissue properties such as elasticity or permeability. Of particular interest is the sensitivity that various MR parameters have to tissue temperature, which allows for the generation of temperature maps that can be used for the monitoring of thermal therapies [2]. Generally, thermal mapping has been implemented using high main magnetic fields as to provide high Signal-to-Noise and overcome some of the challenges present at low field, although high quality low field imaging is an active area of study [3,4]. Should a method be developed (or current methods refined) which provide comparable image quality at low main magnetic field, there is potential for the proliferation in the use of thermal mapping for both diagnostic and interventional applications due to improved accessibility and the reduced cost associated with lower field strength systems.

However, to validate and compare thermal mapping at a variety of field strengths, an MR safe phantom which can track temperature to cross reference with acquisitions from the

scanner is required. In addition, the ability to control the temperature of the phantom is desirable, as this allows for the testing of thermometry during active heating. In this study, we develop a temperature control phantom that can be used to mimic certain tissue properties and can be used to validate and compare different thermal mapping methods.

## Methods:

The body of the phantom was constructed of two nesting Rubbermaid containers (1.5 L and 0.750 L sizes respectively), with the gap between the two providing the insulating effects. To hold the containers in place, a lid was designed in SolidWorks [Dassault Systemes] and 3D printed [Pro2, RAISE 3D] using ABS plastic. The lid also includes a pair of probe insert locations where a fiber optic thermometer can be placed. The NOMAD-Touch [Qualitrol] system was used as the optical thermometer ( $\pm 1^\circ\text{C}$ ;  $\pm 0.1^\circ\text{C}$  Resolution,  $-20$  to  $50^\circ\text{C}$  range, calibrated using a monitored hot water bath). The last component on the lid is a holder for a 10 ohm through hole thin film resistor [Riedon] which can output 50 W of power ( $-55$  to  $155^\circ\text{C}$  operating range,  $\pm 1\%$  tolerance). Once attached to the lid, the resistor was held in place using a plastic screw and the phantom was filled with doped water (1mM  $\text{MnCl}_2$ , 0.163 mM  $\text{CuSO}_4$ , 76.3 mM  $\text{NaCl}$ , corresponding to  $T_1 = 600$  ms,  $T_2 = 150$  ms).

Images were collected on a 0.5 T head only MR scanner [Synaptive Medical Inc.] fitting the phantom and a reference vial inside a human sized head RF array. A Multiple Echo Gradient Echo pulse sequence (matrix size =  $200 \times 110$ , FOV=22cm, slice thickness=3mm, TR=27ms, TE at 7.0, 13.7, and 20.4ms) acquired images over a 21-minute period while 6-minute rounds of current (20V, 1.77A) were applied to the resistor- with a 10 second pull of the paddle mixing mechanism homogenized the temperature throughout- with 3-minute acquisitions between rounds of heating. A custom python pipeline was created to read in the files and match them to the temperature monitored from the NOMAD-Touch system.

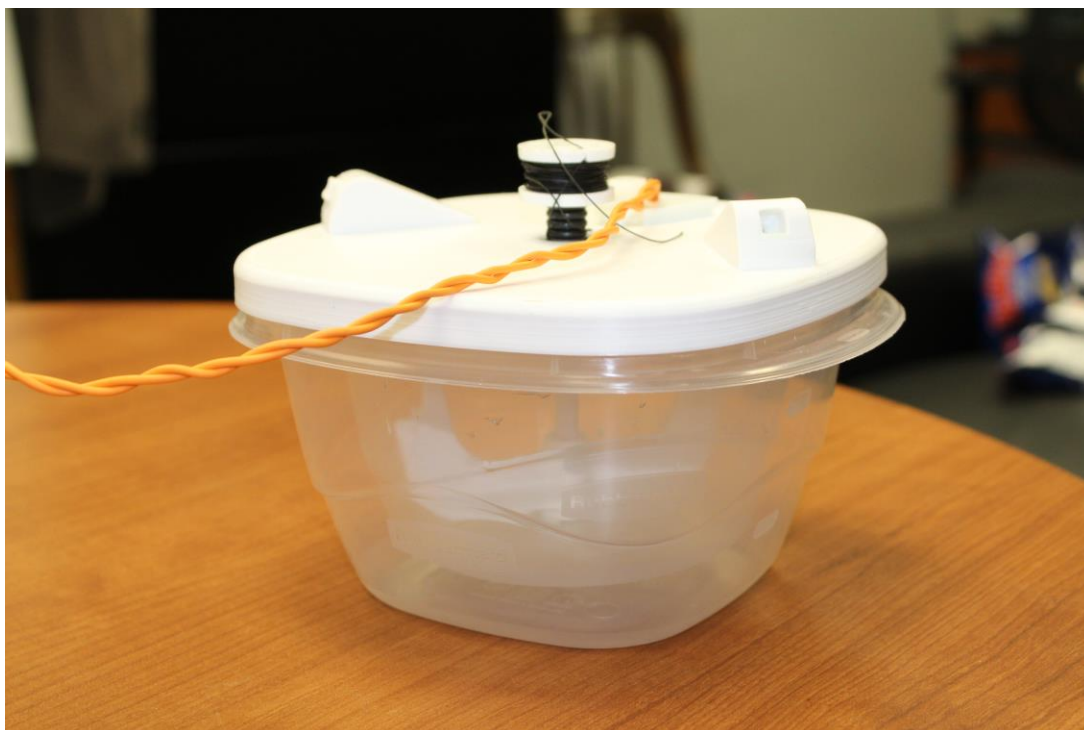


**Figure A.1:** Image of the prototype phantom

Constructed of two containers with an air gap between to insulate from the environment. The spinning paddle was 3D printed and can be spun from outside of the MR suite, allowing for thermal homogenization of the liquid in solution without interfering with the magnet. A resistor placed inside of the liquid could also be operated from outside of the suite, allowing for temperature control.

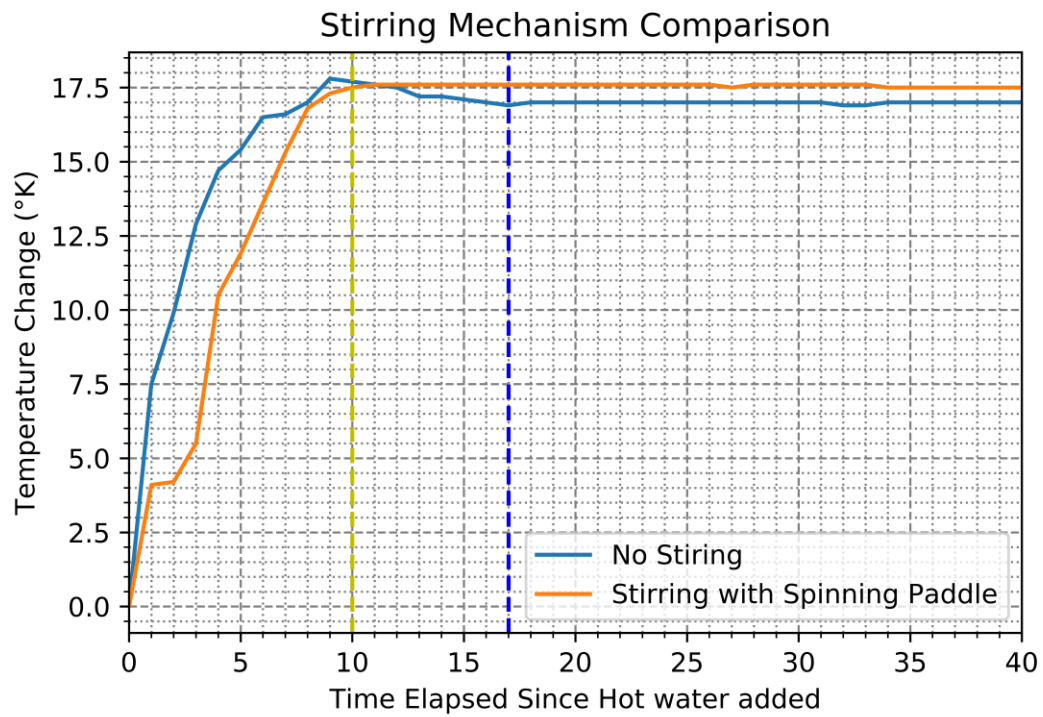


**Figure A.2:** Comparison of thermal homogenization time shown with and without use of a built in stirring mechanism. Equilibrium reached in ~10s using paddle, compared to ~17s without. This verifies the method as a viable remote system for homogenizing the temperature in the phantom.

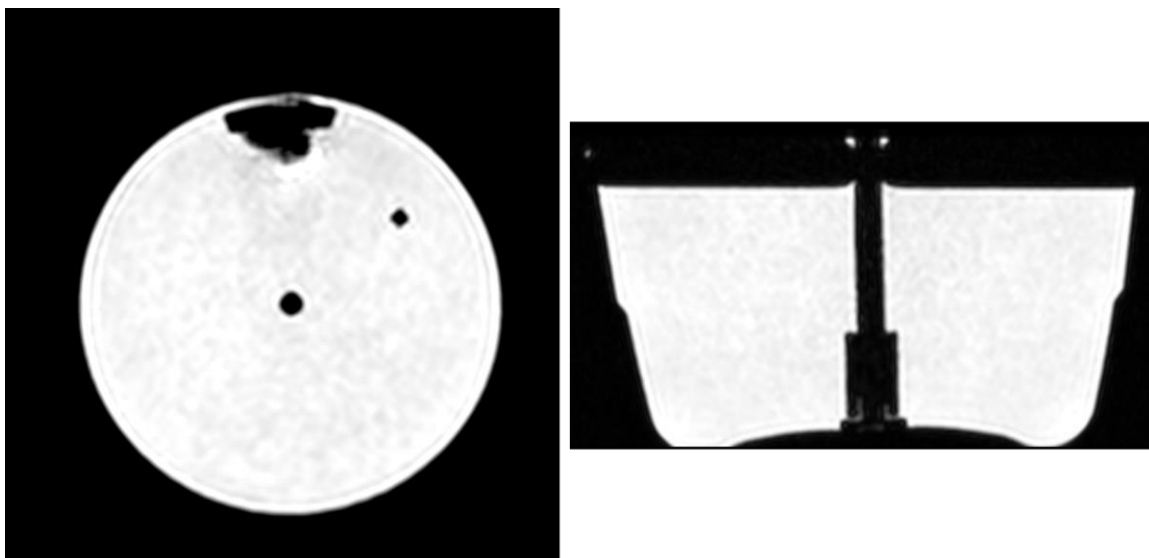


**Figure A.3:** Structural T1 images of the phantom  
Scans conducted on a 0.5T MR system. Left image is a coronal slice and right is axial. Imaging parameters include matrix size = 200x110, FOV=22cm, slice thickness=3mm, TR=27ms, TE at 7.0, 13.7, and 20.4ms. Of note is the susceptibility artefact near the resistor at the top of the coronal slice.

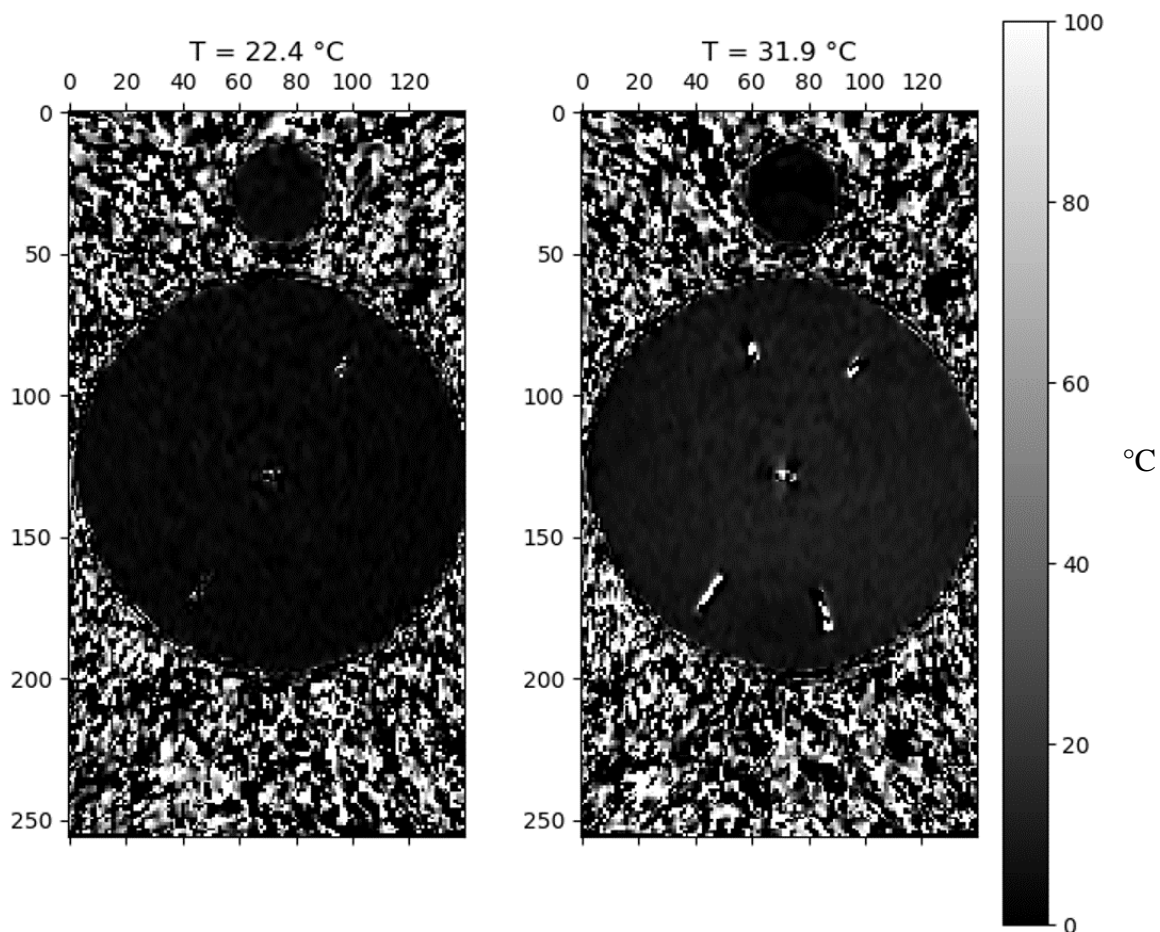


**Figure A.4:** Thermal map comparison of the phantom

Imaging conducted with doped water solution heated to different temperatures as measured by the optical temperature probe inserted into the main body of the phantom. A reference vial filled with doped water was attached to the outside to reference temperature on. The change in signal can be seen at the two temperatures, matching expectation for the change in signal as temperature is altered.



## Results:

The temperature control phantom is shown in **Figure A.1**, with the validation of the homogenization of temperature using the spinning paddle method displayed in **Figure A.2**, guiding the operating protocol of using the stirring mechanism to homogenize the temperature inside the phantom. **Figure A.3** displays a structural MR scan of the phantom using a coronal T1 scan, where the resistor location along with the probe inserts and mixing mechanism can be seen. Further, **Figure A.4** shows the results of a heating test, where the acquisition from a thermometry pulse sequence is compared at two solution temperatures measured on the thermal.

## Discussion & Conclusion:

This study has encompassed both the development and validation of a phantom which has properties favorable for producing thermal maps using MR. By validating the mechanism for homogenizing the temperature (**Figure A.2**), a protocol for remotely mixing the solution so that the temperatures measured using thermometry pulse sequence was confirmed, ensures that the phantom can be set to any temperature, so long as the heating method is consistent. The use of a resistor for heating the phantom proved effective, however as seen in **Figure A.3**, the susceptibility artefacts created by the resistor warrant pause. As the resistors are metallic on the outside, they limit how close measurements can get, as these distortions affect the signal measured in the nearby region. To mitigate this, a high-power ceramic only resistor could be used.

Future improvements involve inclusion of additional probe locations to the lid of the phantom, and full integration of permanent reference vials on the sides. This, along with possible variation of the viscosity of the solution in the phantom will offer more flexibility in controlling the favorable properties for thermometry depending on the specific method used.

Through a simple temperature dependence validation (**Figure A.4**), the phantom adequately matched a Multi-Echo GRE thermometry sequence, and with optimizations to

the acquisition could evaluate the accuracy to which the pulse sequence is able to measure the temperature.

## References:

- [1] R. W. Brown, et al. "Magnetic resonance imaging: physical principles and sequence design." *John Wiley & Sons*, 2014.
- [2] V. Rieke and K. B. Pauly. "MR thermometry." *Journal of Magnetic Resonance Imaging: An Official Journal of the International Society for Magnetic Resonance in Medicine* 27.2 (2008): 376-390
- [3] A. E. Campbell-Washburn, et al. "Opportunities in interventional and diagnostic imaging by using high-performance low-field-strength MRI." *Radiology*, 293(2):384–393, 2019.
- [4] Panther, A., et al. (2019). A Dedicated Head-Only MRI Scanner for Point-of-Care Imaging. ISMRM Proceedings.

## Curriculum Vitae

**Name:** Diego Felipe Martinez

**Post-secondary Education and Degrees:** McMaster University  
Hamilton, Ontario, Canada  
2013-2018 B.Sc.

**Honours and Awards:** Western Graduate Research Scholarship  
2018-2023

International Society for Magnetic Resonance in Medicine  
Educational Stipend Award  
2020-2022

University of Western Ontario, Faculty of Science  
Teaching Assistant Award  
2020

University of Western Ontario, Department of Physics and  
Astronomy  
Teaching Assistant Award  
2019

**Related Work Experience** Teaching Assistant  
The University of Western Ontario  
2018-2023

Teaching Assistant  
McMaster University  
2015-2017

**Publications:**

Shi, R., Mirza, S., Martinez, D. F., Douglas, C., Cho, J., Irish, J. C., Jaffray, D. A., Weersink, R. A., (2020) Cost-function Testing Methodology for Image-Based Registration of Endoscopy to CT images in the Head and Neck. Journal of Physics in Medicine & Biology.